THE ASTROPHYSICAL JOURNAL, 456:566–597, 1996 January 10

COBE[1]/DIRBE OBSERVATIONS OF THE ORION CONSTELLATION FROM THE NEAR- TO FAR-INFRARED

W. F. WALL,[2,3,4] W. T. REACH,[4] M. G. HAUSER,[5] R. G. ARENDT,[6] J. L. WEILAND,[7] G. B. BERRIMAN,[7]
C. L. BENNETT,[3] ELI DWEK,[3] D. LEISAWITZ,[8] P. M. MITRA,[7] STEN F. ODENWALD,[6]
T. J. SODROSKI,[6] AND G. N. TOLLER[7]

Received 1995 January 27; accepted 1995 June 23

ABSTRACT

Observations by the DIRBE instrument aboard the *COBE* spacecraft, collected in 10 wavelength bands spanning the near-infrared to the far-infrared in a 0°.7 beam, are presented for a region covering much of the Orion constellation. For an adopted distance of 450 pc, the total luminosity from dust (from 12 to 240 μm) throughout the Orion A, Orion B, and λ Ori fields, covering 16,900 pc^2, is $\sim 10^6\ L_\odot$. About 24%–36% of this dust luminosity is the result of dust heating by a general interstellar radiation field, with the rest resulting from heating by the Orion OB1 and λ Ori OB associations. Given that the luminosity of the Orion OB1 and λ Ori OB associations is $2.5 \times 10^6\ L_\odot$, and also given that up to $\sim 76\%$ of dust luminosity is caused by dust heated primarily by the Orion stars, $\lesssim 30\%$ of the stellar luminosity is trapped within the clouds and intercloud medium of Orion and reradiated at mid- to far-IR wavelengths.

The near-IR (1.25, 2.2, 3.5, and 4.9 μm) spectral distributions of the Orion Nebula and NGC 2024 indicate the presence of hot ($T \sim$ few $\times 10^2$ K) dust, both because of large $I_\nu(4.9\ \mu\text{m})/I_\nu(1.25\ \mu\text{m})$ ratios and because of a substantial excess in the 3.5 μm band relative to the intensities in the adjacent bands, some of which ($\gtrsim$ 30%) is caused by the 3.28 μm emission line, commonly attributed to polycyclic aromatic hydrocarbons (PAHs).

In the far-IR, the 100, 140, and 240 μm intensities are consistent with a cool (usually 18–20 K, for emissivity index = 2) single-temperature component. The $I_\nu(60\ \mu\text{m})/I_\nu(100\ \mu\text{m})$ color temperature is $\sim$5–6 K higher than that from the cool component, suggesting that an additional warmer component or stochastically heated dust is contributing appreciably to the 60 μm emission. Consequently, dust column densities derived from the 60 and 100 μm intensities, assuming grains in thermal equilibrium, underestimate the dust-to-gas ratio by factors of 5–10. In contrast, the 140 and 240 μm intensities yield dust column densities consistent with reasonable dust-to-gas mass ratios (i.e, $\sim$0.01) to within a factor of 2. However, within this factor of 2, there appears to be a temperature-dependent systematic error in the dust column density derivation.

The results of this paper may apply to external galaxies, since the region studied is more than 200 pc in size. All the above conclusions would have been obtained if the stars and clouds of Orion were placed at the distance of a nearby galaxy ($\sim$1 Mpc) and observed in the DIRBE wavelength bands in an $\sim 1'$ beam (provided the signal-to-noise ratio was unaffected). Hence, observations of the interstellar medium (ISM) in external galaxies that have resolutions of $\sim$100 pc can still yield meaningful results. Further, if the stars and clouds in a spiral galaxy's arms can be represented by a series of Orion star and cloud complexes, one would expect the surface luminosity in the arms (for λ = 12–240 μm) to be 2–4 times that in the interarm regions, averaged over 100 pc scales.

Subject headings: dust, extinction — infrared: ISM continuum — radiative transfer

1. INTRODUCTION

The Orion constellation, jutting $\sim 15°$ out of the Galactic plane, covers nearly 600 deg^2 and contains some of the brightest stars in the sky. Orion is the nearest (450 pc) site of OB star formation and has the nearest giant molecular clouds (see the review by Genzel & Stutzki 1989, and references therein). In addition to the numerous studies that concentrate on the Orion Nebula (M42, NGC 1976), there have been large-scale studies of the stars, gas, and dust in Orion (e.g, see Goudis 1982 and Genzel & Stutzki 1989 for detailed references). Because of Orion's proximity and its intrinsic brightness over a wide range of wavelengths, the stars and clouds of Orion are ideal for studies across the spectrum. This paper concentrates on the two decades in wavelength covering the near-infrared to far-infrared. The Diffuse Infrared Background Experiment (DIRBE) aboard NASA's *Cosmic Background Explorer* (*COBE*) satellite, as part of its all-sky survey, mapped the entire Orion constellation in 10 infrared bands spanning λ = 1.25 μm to 240 μm (Hauser et al. 1991). We present these observations, along with a simple analysis, for a large portion of Orion. The primary goals of the analysis include determining spatial varia-

[1] The National Aeronautics and Space Administration/Goddard Space Flight Center (NASA/GSFC) is responsible for the design, development, and operation of the *Cosmic Background Explorer* (*COBE*). GSFC is also responsible for the development of the analysis software and for the production of the mission data sets. The *COBE* program is supported by the Astrophysics Division of NASA's Office of Space Science and Applications.

[2] Instituto Nacional de Astrofisica, Optica y Electronica, Apdo. Postal 51 y 216 Puebla, Pue., Mexico.
[3] NASA Goddard Space Flight Center, Code 685, Greenbelt, MD 20771.
[4] Universities Space Research Association, NASA Goddard Space Flight Center, Code 685, Greenbelt, MD 20771.
[5] NASA Goddard Space Flight Center, Code 680, Greenbelt, MD 20771.
[6] Applied Research Corporation, NASA Goddard Space Flight Center, Code 685.3, Greenbelt, MD 20771.
[7] General Sciences Corporation, NASA Goddard Space Flight Center, Code 685.3, Greenbelt, MD 20771.
[8] NASA Goddard Space Flight Center, Code 631, Greenbelt, MD 20771.

tions in the properties of interstellar dust—temperature and mass distributions, dust-to-gas mass variations—and investigating the global energetics of this region, including estimates of the proportion of dust heating attributable to the stars of Orion as opposed to the general interstellar radiation field (GISRF, where "general" is meant to refer to a radiation field that applies on much larger size scales than the "local" radiation field; see § 4).

The Orion constellation has been surveyed at many wavelengths. These surveys include the optical surveys of the Orion OB1 and λ Ori associations (e.g., see Blaauw 1964, and references therein; Warren & Hesser 1977, 1978; Murdin & Penston 1977; Brown, de Geus, & de Zeeuw 1994), the radio continuum (Haslam, Quigley, & Salter 1970; Berkhuijsen 1972; Reich 1978), the CO rotational lines (e.g., Tucker, Kutner, & Thaddeus 1973; Kutner et al. 1977; Chin 1978; Maddalena et al. 1986; Sakamoto et al. 1994), the H I 21 cm line (e.g., Heiles & Habing 1974; Chromey, Elmegreen, & Elmegreen 1989; Green 1991; Zhang & Green 1991), the mid- to far-IR with the *Infrared Astronomical Satelite* (*IRAS*) (e.g., Bally, Langer, & Liu 1991; Zhang et al. 1989), and in gamma rays (Bloemen et al. 1984, 1994). The radio continuum surveys (e.g., see Reich 1978; Jonas, de Jager, & Baart 1985) reveal two prominent point sources, Orion A and B, and an $\sim 3°$ circular structure corresponding to the H II region S264, which envelopes the star λ Ori. The Orion A and B radio continuum sources correspond to the H II regions M42 (the Orion Nebula or NGC 1976) and NGC 2024, respectively, and they are located 17° and 19° south of the Galactic plane. The star λ Ori and its H II region are located $\sim 14°$ west-northwest (in Galactic coordinates) of NGC 2024. The molecular clouds associated with Orion A and Orion B are 9°–10° long and $\sim 2°$ wide (~ 75 pc $\times$ ~ 15 pc), with each cloud containing nearly $10^5\ M_\odot$ of molecular hydrogen (Maddalena et al. 1986). An 8° diameter broken molecular ring appears outside the λ Ori H II region, containing $\sim 3 \times 10^4\ M_\odot$ of molecular hydrogen (Maddalena et al. 1986). Maps of atomic gas do not readily reveal the Orion clouds because of confusion from foreground and background gas, unless the maps are either velocity filtered or spatially filtered (e.g., see maps of Green 1991; Chromey et al. 1989; Zhang & Green 1991). In the *IRAS* 100 μm map (e.g., see Bally et al. 1991; Zhang et al. 1989), the Orion A and B molecular clouds are clearly visible, along with a nearly complete 8° diameter dust ring surrounding λ Ori.

The *IRAS* observations were used to investigate the dust properties and the energetics of the Orion region. Bally et al. (1991) examined *IRAS* 60 and 100 μm data and ^{12}CO and ^{13}CO $J = 1 \rightarrow 0$ data in order to compare dust and gas properties in the wide range of radiation field intensities that exist in the clouds of Orion. Bally et al. found that the *apparent* dust-to-gas ratio varied with the radiation field strength, an artifact that could be remedied with a multicomponent grain model. They concluded that such a multicomponent grain model was necessary to interpret the 60 and 100 μm data because small stochastically heated grains make an appreciable contribution to the 60 μm intensity (see Boulanger et al. 1988). Zhang et al. (1989) studied the energetics of the λ Ori dust ring with *IRAS* data and estimated the total far-IR luminosity of the ring and its interior to be $8.6 \times 10^4\ L_\odot$. Zhang et al. concluded that the λ Ori OB association and the GISRF could supply the necessary energy, The DIRBE data permit us to expand upon, and test, the results from the *IRAS* observations.

The purpose of this paper is to present the DIRBE observations of the Orion constellation and a simple model of the global energetics of the region; detailed studies of individual infrared point sources and detailed models of the dust properties in Orion are beyond the scope of this paper. The data processing and preparation are described in § 2. The data are presented in § 3 in the form of surface brightness maps, spectral energy distributions for selected fields, temperature and column density maps from the long-wavelength data, and a map depicting the spatial distribution of a 3.5 μm band excess (possibly caused by the 3.28 μm emission line commonly attributed to polycyclic aromatic hydrocarbons or PAHs). Discussion of the data focuses on the contents of the three large (10°–12°) fields, designated Orion A, Orion B, and λ Ori, and two smaller (2°) fields within the larger fields; the smaller fields contain the Orion Nebula and NGC 2024 (see Table 2). We devote § 4 to the large-scale energetics of Orion, in which we also model the mid- to far-IR spectral energy distribution. Finally, in § 5, the results are discussed in the context of external galaxy observations. Throughout this paper we use an adopted distance of 450 pc, which is consistent with the distance range (320–500 pc) recently determined for the clouds of Orion (Brown et al. 1994).

2. DATA PROCESSING

2.1. *DIRBE Data*

The *COBE* mission and the DIRBE instrument have been described by Boggess et al. (1992) and Silverberg et al. (1993), respectively (see also the *COBE* DIRBE Explanatory Supplement 1995). DIRBE's wavelength bands are listed in Table 1. The instantaneous field of view of the DIRBE instrument is 0.°7 $\times$ 0.°7 in all bands. The 1.25–12 μm bands have been absolutely calibrated using the star Sirius, the 25 μm band using the planetary nebula NGC 7027, 60 and 100 μm bands using Uranus, and 140 and 240 μm bands using Jupiter. The absolute uncertainties of the DIRBE bands are listed in Table 1 and range from 3%–4% in the near-IR bands to 9%–16% in the longer wavelength bands. The band-to-band uncertainty *can be* smaller for bands sharing the same calibrator. For example, the uncertainty in the $I_\nu(140\ \mu\text{m})/I_\nu(240\ \mu\text{m})$ ratio is 6%. In contrast, the uncertainty in the $I_\nu(60\ \mu\text{m})/I_\nu(100\ \mu\text{m})$ ratio is 13%, comparable to the calibration uncertainties in the 60 μm and 100 μm bands themselves. To allow for nonlinearities in the 60 and 100 μm detectors, corrections have been applied to

TABLE 1

DIRBE SPECTRAL BANDS[a]

Spectral Band	λ (μm)	$\Delta\nu_{\rm eff}/\nu$[b]	Uncertainty[c] (%)
1	1.25	0.25	3.8
2	2.2	0.17	4.1
3	3.5	0.25	4.2
4	4.9	0.14	3.4
5	12	0.46	12
6	25	0.37	16
7	60	0.45	9.4
8	100	0.38	14
9	140	0.29	11
10	240	0.40	12

[a] See also *COBE* DIRBE Explanatory Supplement 1995, Table 1.2–1.

[b] Effective fractional bandwidth for $\nu = c/\lambda$ for a source with νI_ν = constant.

[c] Uncertainty in absolute calibration.

the strongest sources in the 60 and 100 μm maps. Specifically, positions in the 60 μm map with intensities surpassing 2100 MJy sr^{-1} were corrected upward by 47%, and positions in the 100 μm map with intensities surpassing 720 MJy sr^{-1} were corrected upward by 56%. These nonlinearity corrections are based on the 60 μm and 100 μm responses to Jupiter compared with those to Uranus (to be discussed in the *COBE* DIRBE Explanatory Supplement 1995). The nonlinearity correction affects fewer than a dozen pixels in the Orion maps.

The DIRBE bandpasses are wide enough (see Table 1) that the instrumental response to a source in a given band depends on the shape of the source spectrum across the bandpass. The *quoted* source brightnesses result from the adoption of a νI_ν = constant source spectrum in computing the effective bandwidth. Color correction factors, defined for DIRBE data as for *IRAS* data (*IRAS* Explanatory Supplement 1988, p. VI-27), allow the conversion from the quoted brightnesses to the true brightnesses for the given source spectrum. The *COBE* DIRBE Explanatory Supplement (1995; Appendix B) lists color correction factors for the DIRBE bands for some representative spectral shapes. In the paper, the DIRBE brightnesses presented in the figures (e.g., Figs. 1, 2, 3, 4, and 6) are not color corrected, but physical quantities derived from the DIRBE brightnesses, such as temperatures and column densities, have been color corrected.

Because the contribution by zodiacal scattering or emission, which we abbreviate as zodiacal "light," varies noticeably from week to week as DIRBE views the sky from different parts of the interplanetary dust cloud, the 1.25 to 100 μm maps were constructed from the brightness of each pixel as observed at a solar elongation angle of 90°. Since the zodiacal light contribution to the longer wavelengths is relatively less appreciable than at wavelengths of 100 μm or shorter, the 140 μm and 240 μm maps were obtained by averaging the 41 weekly maps. All maps were then cleaned of zodiacal light: the zodiacal light in the 1.25 to 100 μm maps was removed using an empirical method in which each ecliptic latitude profile is fitted to a lower envelope of the data (Hauser 1993); in the 140 μm and 240 μm maps, the zodiacal light was approximated by a scaled version of the 25 μm zodiacal light map, 3° × 3° median smoothed, and then subtracted. The 25 μm zodiacal light map was scaled by 0.08 and 0.04 before subtracting from the 140 μm and 240 μm maps, respectively. The scale factors were determined from $I(25\ \mu\text{m})/I(140\ \mu\text{m})$ and $I(25\ \mu\text{m})/I(240\ \mu\text{m})$ ratios binned in ecliptic latitude. The "zodiacal subtraction" at 140 μm and 240 μm reduces the 140 μm and 240 μm emission over most of the Orion A and B molecular clouds and the λ Ori ring by less than 10%.

The resulting Orion maps are presented in Figures 1 and 2 in the equal-area Mollweide projection (see Pearson 1990) in Galactic coordinates, covering the area $l \simeq 180°$ to 230°, $b = -30°$ to $-5°$ or $\alpha(1950) \simeq 4^h10^m$ to 7^h00^m, $\delta(1950) \simeq -20°$ to $+22°$. To remove foreground and background emission associated with the Galactic plane, a cosecant-law background of the form $a_c \csc(|b|)$ was subtracted from the maps, where b is Galactic latitude and a_c is a scale factor. The cosecant-law background was a lower envelope fitted to strips 3° wide on the eastern and western edges of each map and then subtracted from the entire map. To assess the systematic uncertainties associated with the chosen shape for the background, an exponential law of the form $a_e \exp(-c_e|b|)$ was also fitted to the lower envelope of the eastern and western strips, subtracted from the entire map, and compared with the cosecant law–subtracted maps; the fluxes changed by $\lesssim 10\%$. Hence, it is assumed that background subtraction introduces an uncertainty of $\leq 10\%$ at all DIRBE wavelengths. Even though both the cosecant-law and exponential-law background shapes provide only a gross description of the "contaminating" Galactic emission, any small-scale Galactic emission will be dim compared to the bright clouds of Orion.

2.2. H I *and* CO *Maps*

Publicly available H I (Heiles & Habing 1974) and CO (Dame et al. 1987) data sets were gridded to the Mollweide projection to allow comparison with the DIRBE maps. The H I data have a 36′ resolution, and the CO data have a 30′ resolution. Both the H I data and CO data were integrated over the velocity ranges of their surveys. In the gridding process, round-off errors in determining the closest DIRBE pixel on the sky to the given coordinates resulted in gaps in the newly created Mollweide maps. These gaps were filled with the weighted average of the pixel values within a 7 × 7 pixel (2° × 2°) patch centered on a "gap" pixel. The averages were weighted by $1/r^2$, where r is the distance of a given pixel within the patch from the gap pixel. The H I map was further processed by subtracting an exponential-latitude background, of the form $a_e \exp(-c_e|b|)$, which was fitted to the lower envelope of the eastern and western strips in an attempt to isolate the Orion H I emission from the foreground and background H I emission. The cosecant function gave an inadequate representation of the H I background for the Orion map region: there was a strong systematic variation with Galactic latitude in the difference between the data and the fit. The exponential function was a better fit than the cosecant function because the former has two parameters to adjust, whereas the latter has only one. (Note that choosing a particular velocity range of the H I data is not particularly effective in eliminating extraneous material along the line of sight over parts of the map near $l = 180°$, so we adopted background subtraction in order to be consistent across the entire map.) Similar background subtraction for the CO map resulted in virtually no change. The maps are presented in Figure 3; the CO data are presented in a map of velocity-integrated radiation temperature, $\int T_R\,dV$, in units of K km s^{-1}, and the H I data are presented in a map of column density derived from multiplying the integrated brightness temperature by 1.82×10^{18} cm^{-2} (K km s^{-1})$^{-1}$ (Spitzer 1978). Molecular gas column densities are estimated by assuming $N(H_2)/\int T_R\,dV = 2.6 \times 10^{20}$ cm^{-2} (K km s^{-1})$^{-1}$ (see Dame et al. 1987; Dame 1993).

2.3. *Radio Continuum Maps*

Radio continuum maps trace the thermal free-free emission of ionized gas, as well as the nonthermal emission from energetic electrons. However, for the purposes of this paper, ionized gas can be ignored. The masses on the large scales considered here are dominated by dust in the molecular and atomic components of the interstellar medium (ISM). The effect on the dust energetics of ionized gas is largely from resonantly scattered Lyα photons heating the dust grains. Data from the Rhodes/HartRAO 2300 MHz radio continuum survey (Jonas, Baart, & Nicolson 1995; Jonas et al. 1985) can be used to set limits on the contribution of Lyα heating to the dust luminosity in Orion. For the Orion Nebula, we find that only $\simeq 10\%$–15% of the mid- to far-IR luminosity could be caused by Lyα heating of dust grains, assuming that *all* the 2300 MHz

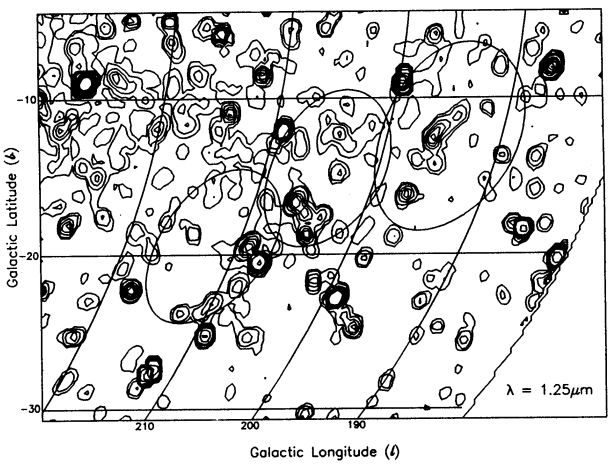

FIG. 1*a*

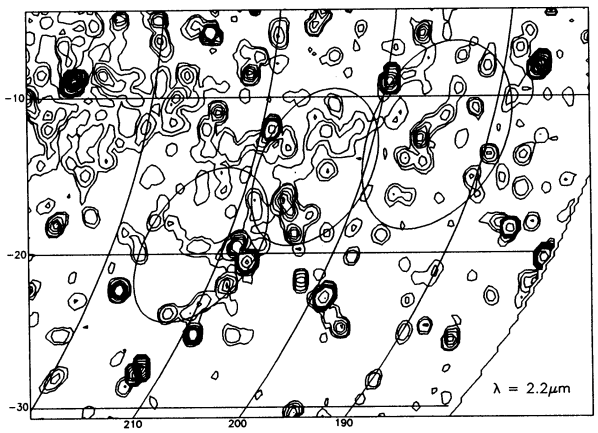

FIG. 1*b*

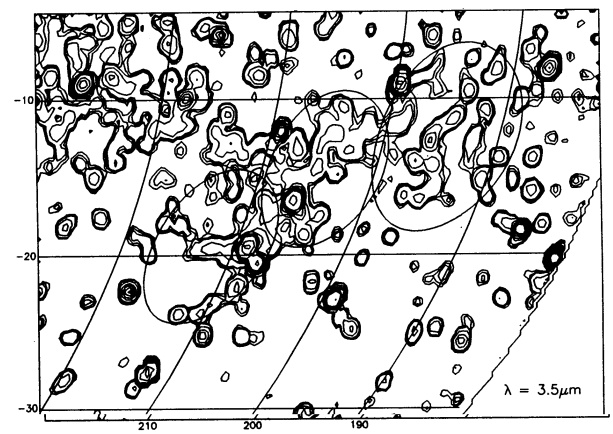

FIG. 1*c*

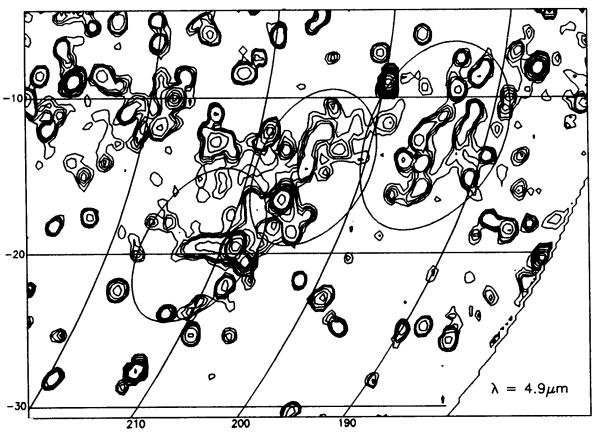

FIG. 1*d*

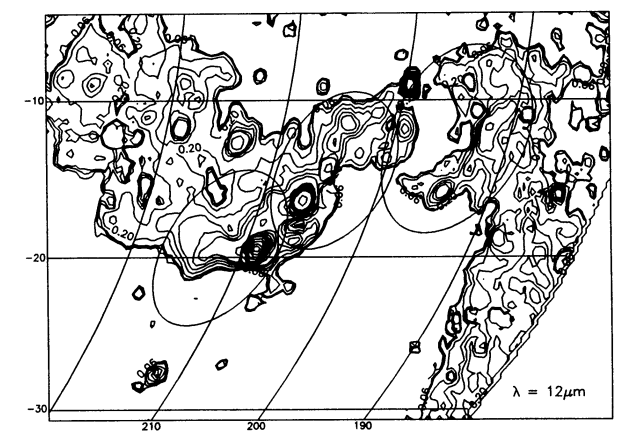

FIG. 1*e*

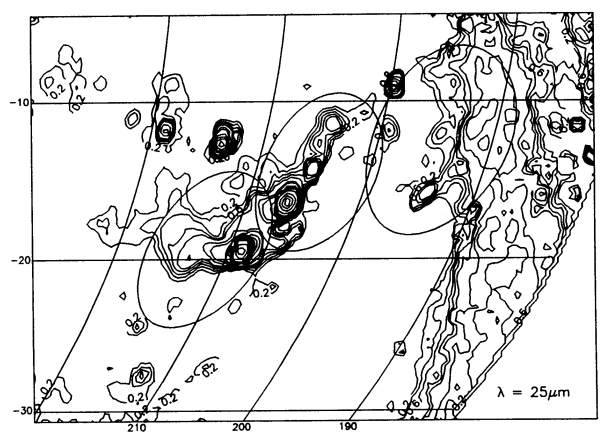

FIG. 1*f*

FIG. 1.—The DIRBE surface brightness maps for $\lambda = 1.25$ to 240 μm are displayed in the equal-area Mollweide projection with a Galactic longitude-latitude coordinate grid. The analysis concentrates on the three 10°–12° circular fields that appear in the map as roughly elliptical loops; circles on the sky appear distorted in this projection. The fields, from east to west, are the Orion A, Orion B, and λ Ori fields. Contained within the Orion A and Orion B fields are the 2° Orion Nebula and NGC 2024 fields (see Table 2 and Fig. 2 for details). The absolute photometric uncertainty in the maps varies from 3% to 16%, depending on the map's wavelength (see Table 1). All maps have been "cleaned" of zodiacal light and had cosecant ($|b|$) backgrounds subtracted. The lowest contour level in each map is 2–3 σ, where σ is the photometric rms noise. The effective wavelength of each map and the contour levels are as follows: (*a*) $\lambda = 1.25$ μm, contour levels = 0.1, 0.2, 0.4, 0.6, 0.8, 1, 2, 3, 4, 5, 6, 7, 8, 9, 10, 20, 40, 60, 80, and 100 MJy sr^{-1}. (*b*) $\lambda = 2.2$ μm, contour levels = 0.1, 0.2, 0.4, 0.6, 0.8, 1, 2, 3, 4, 5, 6, 7, 8, 9, 10, 20, 40, 60, and 80 MJy sr^{-1}. (*c*) $\lambda = 3.5$ μm, contour levels = 0.06, 0.08, 0.1, 0.2, 0.4, 0.8, 1, 2, 3, 4, 5, 6, 7, 8, 9, 10, 20, 40, and 60 MJy sr^{-1}. (*d*) $\lambda = 4.9$ μm, contour levels = 0.04, 0.06, 0.08, 0.1, 0.2, 0.4, 0.6, 0.8, 1, 2, 3, 4, 5, 6, 7, 8, 9, 10, 15, and 20 MJy sr^{-1}. (*e*) $\lambda = 12$ μm, contour levels = 0.06, 0.08, 0.1, 0.2, 0.4, 0.6, 0.8, 1, 2, 3, 4, 5, 6, 7, 8, 9, 10, 20, 30, 40, 50, and 60 MJy sr^{-1}. (*f*) $\lambda = 25$ μm, contour levels = 0.1, 0.2, 0.4, 0.6, 0.8, 1.0, 1.5, 2.0, 4, 6, 8, 10, 20, 40, 60, 80, 100, 200, and 300 MJy sr^{-1}. (*g*) $\lambda = 60$ μm, contour levels = 0.6, 1, 2, 4, 6, 8, 10, 20, 40, 60, 80, 100, 200, 400, 600, 800, 1000, and 2000 MJy sr^{-1}. (*h*) $\lambda = 100$ μm, contour levels = 2, 4, 6, 8, 10, 15, 20, 30, 40, 60, 80, 100, 200, 400, 600, 800, 1000, 1500, and 2000 MJy sr^{-1}. (*i*) $\lambda = 140$ μm, contour levels = 5, 10, 15, 20, 30, 40, 60, 80, 100, 150, 200, 400, 600, 800, 1000, 1500, and 1900 MJy sr^{-1}. (*j*) $\lambda = 240$ μm, contour levels = 3, 5, 10, 15, 20, 30, 40, 60, 80, 100, 150, 200, 250, 300, 350, 400, 450, 500, 550, 600, 650, 700, and 750 MJy sr^{-1}.

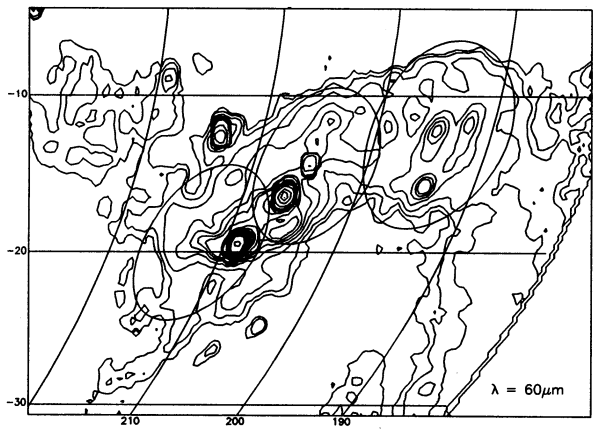

FIG. 1*g*

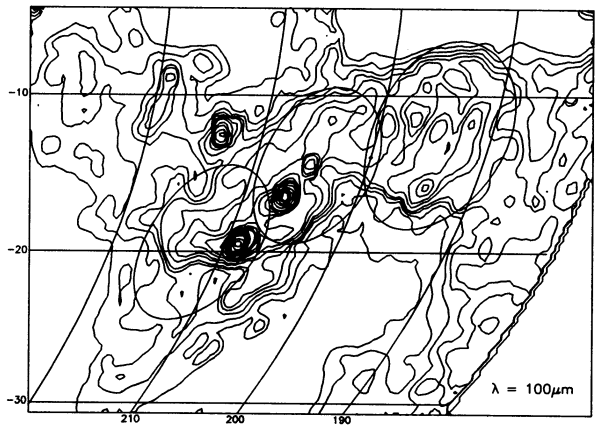

FIG. 1*h*

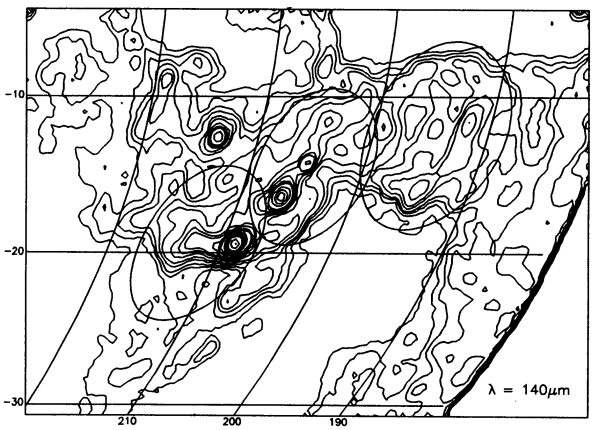

FIG. 1*i*

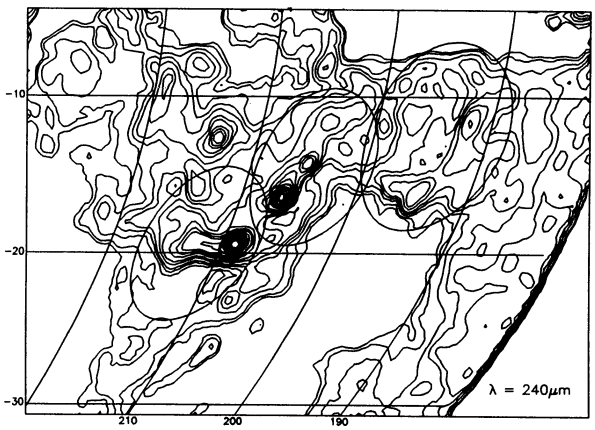

FIG. 1*j*

emission is thermal free-free emission. Hence, for the large areas (hundreds to thousands of square parsecs) considered in this paper, it is likely that the ionized gas plays only a minor role in the energetics. The distribution of masses between the three components of the ISM is discussed in § 3.3.

3. RESULTS

All the results and discussions in this paper concentrate on three large circular fields (diameter = 10°–12°) and two smaller fields (diameters = 2°) contained within the larger fields (see Table 2). The fields represent a swath roughly 30° long and 10° wide (~240 pc × 80 pc) or a solid angle of 0.083 sr (16,900 pc^2), roughly half the Orion constellation (0.18 sr). The larger fields were chosen to enclose prominent molecular clouds or features (i.e., Orion A and B molecular clouds and the λ Ori Ring), and the smaller fields contain the H II regions NGC 2024 and the Orion Nebula (M42/43).

3.1. *Maps*

3.1.1. *Near-IR Maps*

The near-IR maps (λ = 1.25, 2.2, 3.5, and 4.9 μm) in Figures 1*a*–1*d* show point sources superposed on underlying faint diffuse emission (<0.3–0.4 MJy sr^{-1}). (Note: Any portion of this lower level emission could be unresolved point sources, but, for this discussion, the lower level emission is considered

TABLE 2

THE ORION FIELDS

FIELD PARAMETERS	FIELDS				
	Orion Nebula	Orion A	NGC 2024	Orion B	λ Ori
Center (*l*, *b*)	209°.1, −19°.4	212°.0, −19°.4	206°.3, −16°.5	204°.4, −14°.5	194°.5, −12°.5
Diameter					
Degrees	2	10	2	10	12
Parsecs[a]	16	79	16	79	94
Area					
Steradians	1.1×10^{-3}	2.5×10^{-2}	1.1×10^{-3}	2.5×10^{-2}	3.6×10^{-2}
(Parsecs)^2[a]	2.1×10^{2}	5.1×10^{3}	2.1×10^{2}	5.1×10^{3}	7.3×10^{3}

[a] For adopted distance of 450 pc.

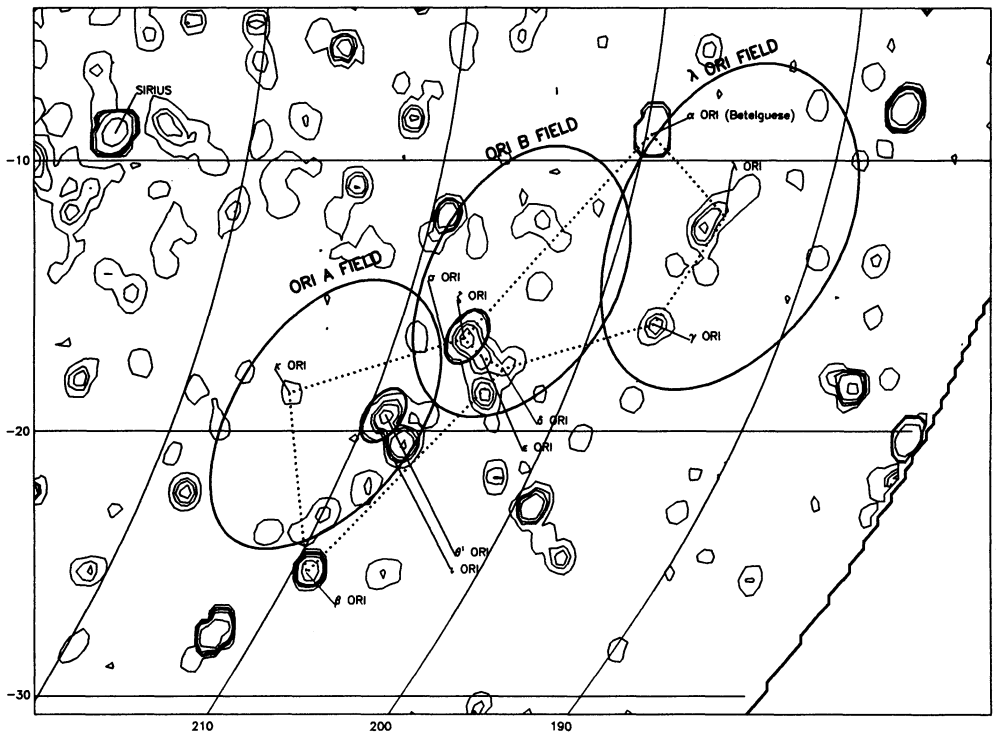

FIG. 2*a*

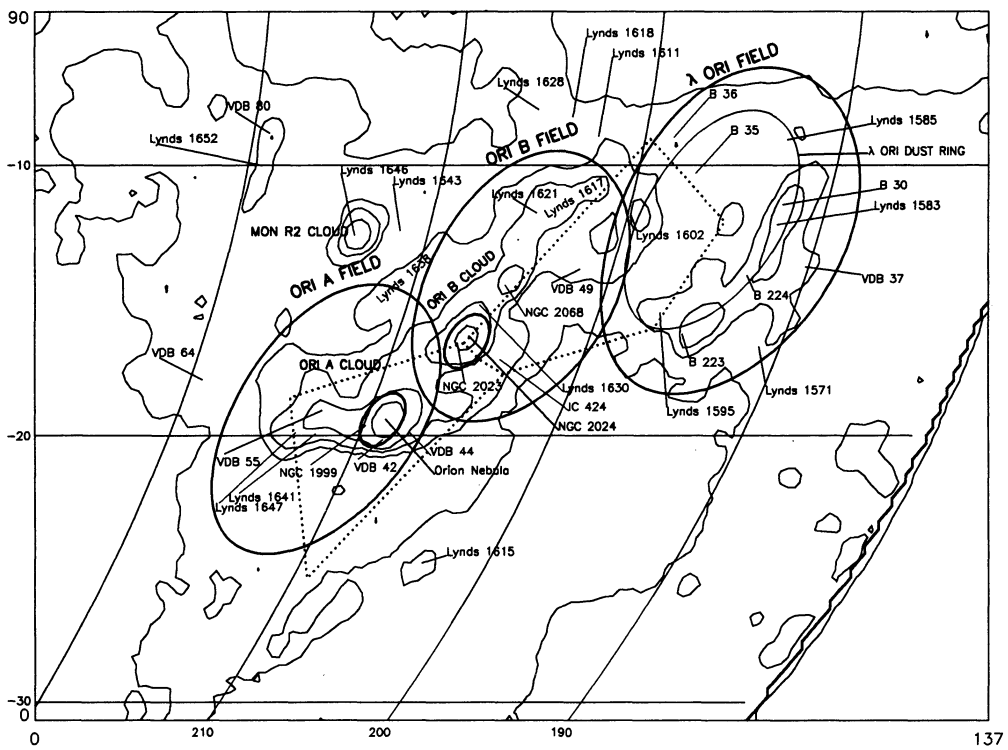

FIG. 2*b*

FIG. 2.—Sparsely contoured maps are used to illustrate the contents of the Orion maps. (*a*) A near-infrared map shows the positions of the major stars of Orion. "Orion the Hunter" is depicted as a dotted outline. The Orion A, Orion B, and λ Ori fields, which correspond to circles on the sky (but are distorted by the projection), are displayed with thick solid lines. The smaller Orion Nebula and NGC 2024 fields are seen here centered on θ^1 Ori and ζ Ori, respectively. (*b*) A far-infrared map shows positions of some clouds in the Orion map. Orion the Hunter and the circular fields are shown again for orientation. The solid line representing the λ Ori dust ring was measured from an *IRAS* image (Zhang et al. 1989). For more on the Lynds dark clouds and the VDB reflection nebulae, see Lynds (1962) and van den Bergh (1966), respectively. For a more complete listing of features, see Maddalena et al. (1986, Fig. 3).

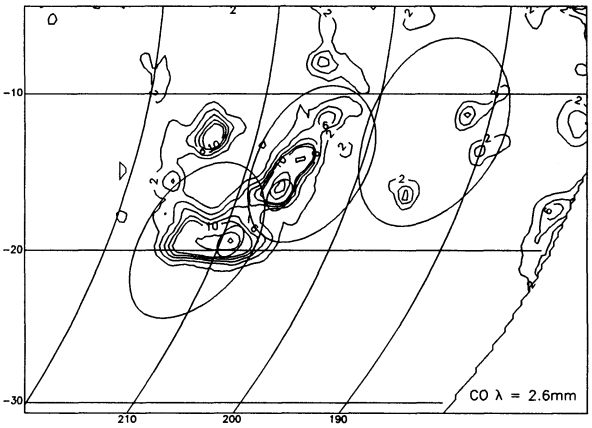

FIG. 3a

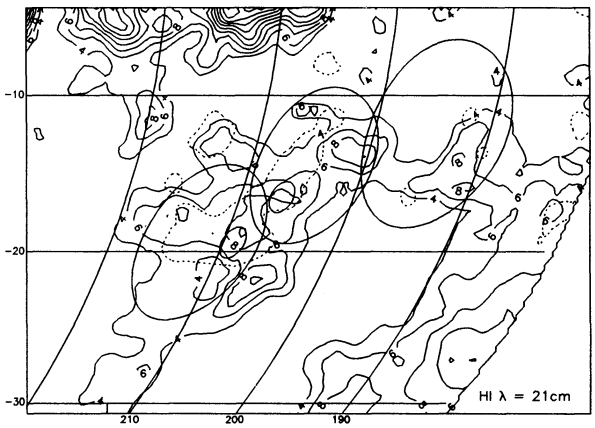

FIG. 3b

FIG. 3.—Publicly available CO and H I data gridded onto the Mollweide projection are shown. The circular Orion A, Orion B, and λ Ori field and the smaller Orion Nebula and NGC 2024 fields are depicted as quasi-elliptical loops. (*a*) A velocity-integrated CO $J = 1$–0 map from the GISS Survey (Dame et al. 1987; Maddalena et al. 1986) is shown. Background subtraction changed the map negligibly and was thus deemed unnecessary. The contour levels are 2, 4, 6, 8, 10, 20, 30, 40, and 50 K km s^{-1}. (*b*) A velocity-integrated H I 21 cm map from the Heiles & Habing (1974) survey is shown. An exponential background in the form of $a_e \exp(-c_e|b|)$, was subtracted from the map, in order to isolate the Orion clouds. The contours are given as column densities, N(H I), with levels 4, 6, 8, 10, 12, 14, 16, 18, and 20 × 10^{20} cm^{-2} Dashed contour represents the positions of the molecular clouds.

to be diffuse emission.) The proportion of near-IR emission in discrete DIRBE point sources is roughly constant with near-IR wavelength, ~60% at $\lambda = 1.25$ μm and ~50% at $\lambda = 4.9$ μm, even though the number of point sources declines by factors of 2–3 in going from $\lambda = 1.25$ to 4.9 μm. The wavelength dependence of the number of detected discrete point sources neither tightly constrains, nor is tightly constrained by, the stellar spectral and luminosity classes. Combinations of stellar spectral types, such as assuming that half the point sources are early spectral types (e.g., B supergiants) and the other half late spectral types (e.g., M giants or M supergiants), could account for the declining point source number with increasing wavelength, except that only ~1% of the stars in the OB associations have spectral types K0 or later (Warren & Hesser 1977; Murdin & Penston 1977). Another possibility is if approximately half the discrete point sources each represent *single* early-type (e.g., B) supergiants and half the discrete point sources each represent *two* early-type supergiants. In both these cases, the number of DIRBE point sources with fluxes exceeding the DIRBE point source detection limit at $\lambda = 1.25$ μm is 2–3 times that for the corresponding number at $\lambda = 4.9$ μm. (The point source limit is 30 Jy for $\lambda = 1.25$–4.9 μm; see *COBE* DIRBE Explanatory Supplement 1995.) Note that we are not ruling out cases involving intermediate spectral types in accounting for the near-IR wavelength dependence of the number of point sources.

Some of the point sources are coincident with the major stars of Orion (see Fig. 2), such as α, λ, γ, δ, ε, ζ, β, and κ, where there is blending of the belt stars (δ, ε, ζ) contours. Note also that some point sources may represent clusters of stars: the θ^1 source is coincident with the Orion OB1d subassociation (see Kutner et al. 1977). Prominent sources exist at near-IR wavelengths where there are no prominent stars ($m_v \lesssim 4$) at visible wavelengths. For instance, immediately southwest of θ^1 at $l = 208°$, $b = 20.^{\circ}5$ is a source that is about as bright in the near-IR as the θ^1 source itself, even though no bright stars ($\lesssim 4$ mag) in the V band are found.

Among the structures seen in the diffuse emission is a ~5° long arc along the southwest edge of the Orion A field, a "tongue" pointing eastward from θ^1, and a ridge snaking through the λ Ori field and centered on the λ Ori star. The Orion A "tongue" contains a number of *IRAS* point sources, many of which appear to be young stellar objects (Chen & Tokunaga 1994). The increasing apparent length of the "tongue" and the λ Ori ridge with increasing wavelength is partly an artifact of the lower contours used in the longer wavelength maps.

The fraction of near-IR emission, from both point sources and "diffuse" emission, that is caused by scattering (as opposed to direct star light or thermal dust emission) can be crudely estimated from the scattering optical depth per unit gas column density [i.e., $\tau_s(1.25\ \mu m)/N(H) = 7.7 \times 10^{-23}$ cm^2, $\tau_s(2.2\ \mu m)/N(H) = 9.4 \times 10^{-24}$ cm^2, $\tau_s(3.5\ \mu m)/N(H) = 1.4 \times 10^{-24}$ cm^2; Draine & Lee 1984]. Assuming the local value for the interstellar radiation field at $\lambda = 1.25$, 2.2, and 3.5 μm [with near-IR mean intensities of $I_\nu(1.25\ \mu m) = 0.42$ MJy sr^{-1}, $J_\nu(2.2\ \mu m) = 0.49$ MJy sr^{-1}, $J_\nu(3.5\ \mu m) = 0.32$ MJy sr^{-1}; Mathis, Mezger, & Panagia 1983] and using the column densities averaged over each of the Orion fields implies that 30%–70% of the 1.25 μm emission, 7%–10% of 2.2 μm emission, and <1% of the 3.5 μm emission are scattered. These scattering fractions are lower limits, since the contribution of the Orion stars to the near-IR mean intensities has not been included.

3.1.2. *Mid-IR and Far-IR Maps*

The mid-IR ($\lambda = 12, 25$ μm) and far-IR ($\lambda = 60, 100, 140, 240$ μm) maps in Figures 1*d*–1*j* show extended structures with only a few prominent point sources: the Orion Nebula, NGC 2024, NGC 2068, and Mon R2 (see Fig. 2*b*). The star α Ori is still visible in the 12, 25, and 60 μm maps (see Figs. 1*e*–1*g* and 2*a*). The Orion A and B clouds form an apparently continuous structure punctuated by the Orion Nebula, NGC 2024, and NGC 2068 point sources. Further west, the λ Ori Ring, which is seen very clearly in the *IRAS* maps (see Zhang et al. 1989), has a thicker, more broken appearance in the big DIRBE beam (see Figures 1*h*–1*j* and 2*b*).

To estimate the total luminosity of interstellar dust thermal emission, the 12–240 μm maps were added together to generate surface luminosity maps. (The 12 μm band intensities are prob-

ably dominated by dust emission rather than stellar emission, since an extrapolation of the near-infrared intensities for the five fields—see Figure 5—suggests that stellar emission contributes less than ~10%–20% of the total 12 μm fluxes.) The surface luminosity, $\mathscr{L}$, in each pixel was derived according to

$$\mathscr{L}(12\text{–}240\ \mu\text{m}) = 4\pi \sum_{j=5}^{9} \frac{1}{2} (\nu_{j+1} I_{j+1} + \nu_j I_j) \ln\left(\frac{\nu_j}{\nu_{j+1}}\right), \quad (1)$$

which is an approximation to

$$\mathscr{L}(12\text{–}240\ \mu\text{m}) = 4\pi \int_{c/240\ \mu\text{m}}^{c/12\ \mu\text{m}} \nu I_\nu \, d(\ln \nu) . \quad (2)$$

The I_j is the intensity or surface brightness in DIRBE band j, ν_j is the frequency in DIRBE band j, where $j = 5$–10 corresponds to $\lambda = 12$, 25, 60, 100, 140, and 240 μm, and c is the speed of light. The luminosity, L(12–240 μm), of a source of area A(pc^2) is $\mathscr{L}$(12–240 μm)A. The $\mathscr{L}$(12–240 μm) map is shown in Figure 4 and is in units of $L_\odot$ pc^{-2}, where 1 $L_\odot$ pc^{-2} corresponds to a frequency-integrated surface brightness of 32 nW m^{-2} sr^{-1}. It is assumed that the uncertainty in the DIRBE broadband luminosities is 16%, the maximum of the uncertainties over the 12–240 μm bands (see Table 1). To estimate crudely the color corrections, we adopted a simplified shape for the spectral distributions averaged over each of the Orion fields (Orion A, Orion B, λ Ori, Orion Nebula, and NGC 2024): piecewise linear in νI_ν versus log ν (i.e., the shapes visible in Fig. 5). The resulting color corrections increased the luminosities of the Orion fields by only 5%–11%. Thus, it is not unreasonable to assume that the color corrections for the luminosities of most of the individual pixels in the Orion fields can be ignored (at the $\lesssim$10% level).

The interstellar dust luminosities, L(12–240 μm), of the five fields are listed in Table 3 for the adopted distance of 450 pc. Notice that the luminosity over the full DIRBE wavelength range, L(1–240 μm), is within ~10% of L(12–240 μm). Using the 140 and 240 μm intensities and assuming a ν^β emissivity law, with $\beta = 2$, to extrapolate to longer wavelengths suggests that L(12–240 μm) represents >90% of the dust emission. Extrapolating the 140 and 240 μm intensities back to a wavelength of 12 μm, again assuming a ν^2 emissivity law, results in an L(12–240 μm) that is only ~70% of that observed. This is expected if the extrapolated L(12–240 μm) is dominated by large (~0.01–0.1 μm) equilibrium-heated grains, while L(12–60 μm) is dominated by small stochastically heated grains. Hence, adding the observed L(12–60 μm) to be extrapolated L(12–240 μm) should give the observed L(12–240 μm) and does to within 7% (see Table 3). The luminosities over the wavelength range covered by *IRAS*, L(12–100 μm), are ~60% of the 12–240 μm luminosity, as predicted by Boulanger & Pérault (1988). For the λ Ori field, however, L(12–100 μm)/L(12–240 μm) = 0.4. Thus, one might expect estimates of the full (i.e., mid-IR + far-IR) dust luminosity from the λ Ori field to be too small, based on extrapolations of the *IRAS* data. However, the *IRAS* 60 & 100 μm data overestimate the 60 and 100 μm intensities relative to DIRBE (see *COBE* DIRBE Explanatory Supplement 1995), roughly canceling out the faulty extrapolation for the λ Ori field. For the λ Ori dust ring *and its interior*, Zhang et al. (1989) obtain a dust luminosity of 1.1 × 10^5 $L_\odot$ (adjusting from their adopted distance of 400 pc to our adopted distance of 450 pc), whereas the DIRBE value is 1.5 × 10^5 $L_\odot$. The absolute calibration uncertainties of DIRBE and *IRAS*, 16% for DIRBE broadband luminosities and 20% for *IRAS*, and differ-

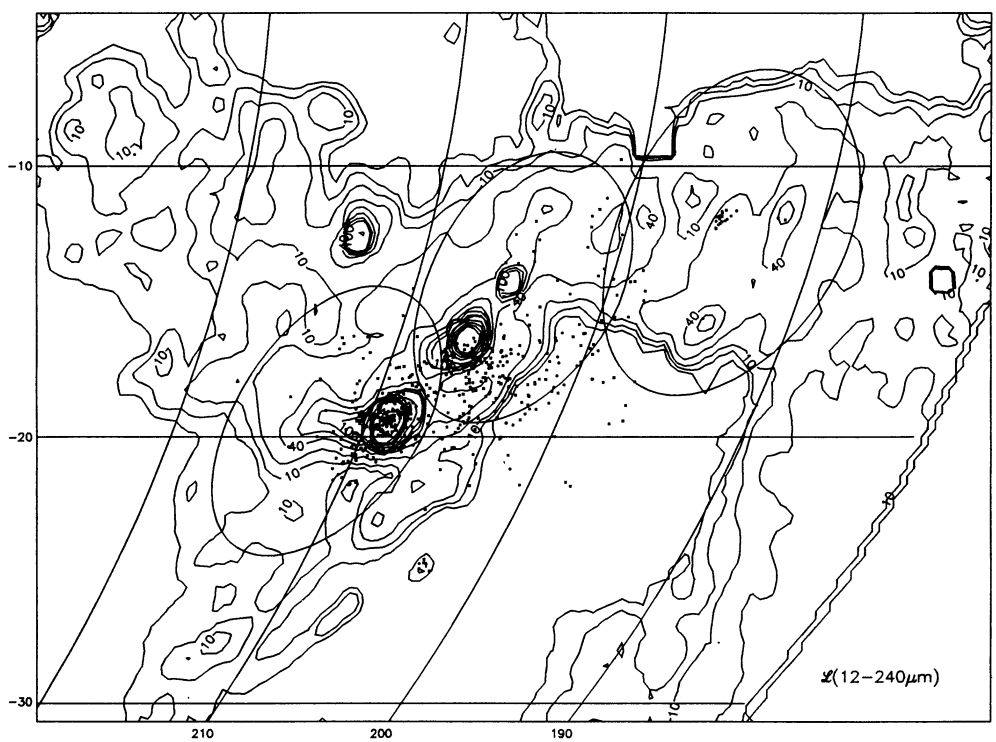

FIG. 4.—The surface luminosity, integrated over $\lambda = 12$–240 μm, is shown. Dots represent the positions of the stars in Orion OB1 and λ Ori OB associations (Warren & Hesser 1977; Murdin & Penston 1977). This map is in units of $L_\odot$ pc^{-2}, where each $L_\odot$ pc^{-2} of surface luminosity corresponds to 32 nW m^{-2} sr^{-1} of surface brightness. The contour levels are 3, 6, 10, 20, 40, 60, 80, 100, 200, 400, 600, 800, 1000, 3000, and 5000 $L_\odot$ pc^{-2}. Uncertainties in the surface luminosities attributable to the calibration uncertainties are 16%. (The α Ori data have been excised from the map, since α Ori is not part of the Orion OB1 association.)

TABLE 3

INFRARED LUMINOSITIES OF ORION FIELDS

WAVELENGTH RANGE (μm)	LUMINOSITY[a] ($L_\odot$)					
	Orion Nebula	Orion A	NGC 2024	Orion B	λ Ori	Combined[b]
12–240[c]	3.6×10^5	5.0×10^5	1.4×10^5	2.9×10^5	1.5×10^5	9.4×10^5
12–100[c]	2.8×10^5	3.4×10^5	9.7×10^4	1.6×10^5	6.4×10^4	5.7×10^5
1–240[c]	3.8×10^5	5.7×10^5	1.5×10^5	3.5×10^5	1.8×10^5	1.1×10^6
(12–240)[d]	1.6×10^5	2.9×10^5	8.2×10^4	2.2×10^5	1.3×10^5	6.2×10^5
12–60[c]	1.8×10^5	2.2×10^5	6.4×10^4	9.0×10^4	3.4×10^4	3.4×10^5
3X[e]	4.1×10^2	6.7×10^2	4.4×10^2	9.8×10^2	3.6×10^2	2.0×10^3
OB[f]	5.0×10^5	8.3×10^5	3.5×10^5	1.4×10^6	2.9×10^5	2.5×10^6

[a] A distance of 450 pc is assumed.
[b] Combined Orion A + Orion B + λ Ori field.
[c] Uncertainty of $\pm$ 16%.
[d] Extrapolated from 140 and 240 μm fluxes, assuming $\beta = 2$.
[e] 3.5 μm band excess (see § 3.4).
[f] Luminosities of the Orion OB1 and λ Ori OB associations (see Warren & Hesser 1977; Murdin & Penston 1977; § 3.1.2).

ences in treatment of the background could easily account for this minor discrepancy.

OB stars, over their lives, destroy portions of the clouds in which they form. Once this occurs, much of their radiated energy is lost to interstellar space. Indeed, the Orion Nebula itself is a "blister" H II region on the near side of the Orion A molecular cloud, with its ionized gas and the ionizing radiation escaping in a "champagne flow" fashion (Zuckerman 1973; Tenorio-Tagle 1979). Given the age of the Orion OB1 and λ Ori OB associations (1–11 $\times$ 10^6 yr; Brown et al. 1994, Murdin & Penston 1977), Leisawitz & Hauser (1988) would predict 10%–25% of the OB star energy to be absorbed within 40 pc of the star. The DIRBE infrared observations of the Orion clouds are consistent with the Leisawitz & Hauser estimate, which is supposed to apply to an average evolved OB cluster environment. Figure 4 shows the positions of the stars of the Orion OB1 and λ Ori OB associations (Warren & Hesser 1977; Murdin & Penston 1977). The luminosities of the stars were estimated from their spectral types, V-magnitudes, $B-V$ colors, the visual extinctions, and the adopted distance of 450 pc. Note that we use these luminosities estimated from spectral types even though Brown et al. (1994) give explicitly the luminosities of the Orion OB1 stars in their Table 1. The Brown et al. (1994) photometry, based on the Walraven photometric system, can underestimate the luminosities of the early-type stars that dominate the energetics of the region by factors of $\sim$2 (A. G. A. Brown, private communication; Brown et al. 1994, and references therein). The derived luminosities for a few stars (δ, ϵ, ζ, θ^1, ι, κ, and λ) were compared with those listed in Snow & Morton (1976) and agreed to within $\pm$30%. The stellar luminosities within the Orion fields totals 2.5 $\times$ 10^6 $L_\odot$ (see Table 3). Hence, $\sim$40% of the stellar luminosity is trapped within the clouds and intercloud medium of Orion and reradiated as mid- to far-IR, assuming no contribution by the general interstellar radiation field (GISRF) to dust heating. If the GISRF is responsible for one-third of the dust heating (see § 4), then only $\sim$25% of the stellar luminosity is trapped and reprocessed.

3.2. *Spectral Distributions*

The spectral distributions of the five fields are displayed in Figure 5. The spectral distributions are expressed as νL_ν, rather than L_ν, because νL_ν gives the energy per logarithmic frequency interval, since $L_\nu d\nu = \nu L_\nu d \ln \nu$, and it has the advantage that $\nu L_\nu = \lambda L_\lambda$. The general shape of the spectral distributions, with some exceptions, is a decline from 1.25 μm to 4.9 μm (representing the declining stellar emission) and an increase from 4.9 μm to a peak at 60, 100, or 140 μm (representing the rising dust emission) followed by a decline at 240 μm. The exceptions to the basic shape include the pronounced 3.5 μm excess evident in the Orion Nebula and NGC 2024 fields and 12–25 μm plateau visible in the Orion B and λ Ori fields. Based on *IRAS* observations of the California Nebula (Boulanger et al. 1988), the 12–25 μm plateau appears to be the value expected far from an H II region, but the low value of νI_ν(12 μm)/νI_ν(25 μm) (=0.4) inside the Orion Nebula field appears to be the value expected inside an H II region. The 3.5 μm excess is probably caused by hot stochastically heated dust (i.e., $T \sim$ few $\times$ 10^2 K during the time the grains are emitting appreciably in the near-IR) continuum emission or possibly caused by the 3.3 μm PAH line (see § 3.4).

The 1.25, 2.2, and 4.9 μm intensities in the H II region fields, Orion Nebula and NGC 2024, suggest hot dust emission in the 4.9 μm band. The near-IR spectral distribution is considerably shallower than the sample Galactic spectral distribution in the near-IR (see Fig. 5 and also see Arendt et al. 1994 for typical Galactic plane near-IR colors). While the Galactic near-IR spectral distribution is consistent with a mix of late and early spectral type stars, the Orion Nebula and NGC 2024 near-IR spectral distributions cannot be matched by stars of any spectral type even when including the effects of extinction (i.e., applying the Rieke & Lebofsky 1985 reddening law): any combination of spectral type and extinction that matches the observed I_ν(2.2 μm)/I_ν(1.25 μm) will underestimate the observed I_ν(4.9 μm)/I_ν(1.25 μm) by factors $>$4. However, it is possible to match the near-IR I_ν(2.2 μm)/I_ν(1.25 μm) and I_ν(4.9 μm)/I_ν(1.25 μm) ratios in the Orion Nebula, for example, by using a combination of *extinctions*: one heavily obscured ($A_V = 30$ mag or $A_J \simeq 9.2$ mag) cluster of stars that dominates at 4.9 μm and a naked cluster that dominates at 1.25 and 2.2 μm. This implies that the obscured stars would be intrinsically $\sim$60 times as luminous as the naked cluster to give the required dominance at 4.9 μm. Since the observed stellar luminosity in the Orion Nebula field is 5 $\times$ 10^5 $L_\odot$ (Table 3), there would have to be an obscured cluster of stars with a luminosity of 3 $\times$ 10^7 $L_\odot$, about 2 orders of magnitude greater than the

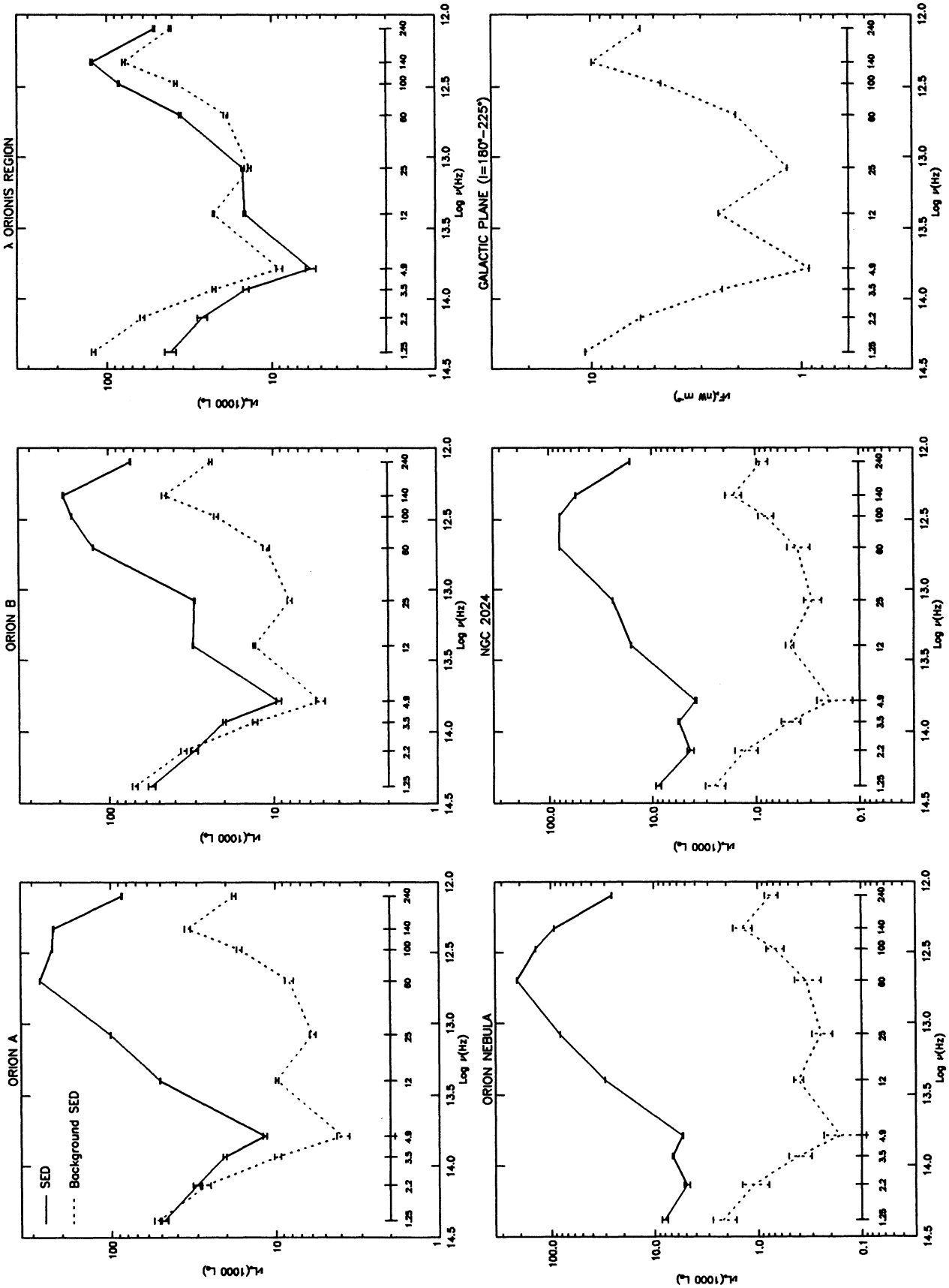

FIG. 5.—The spectral energy distributions (SEDs) of the Orion fields are displayed as νL_ν vs. log (ν) (a wavelength scale in units of microns is also shown). Solid lines represent the SED after the background subtraction. Dashed lines represent the SED of the background itself. An SED of the Galactic plane ($l = 180°$–$225°$, $b = -0.3$ to $+0.3$) is shown for comparison with the background SEDs. Error bars represent 5 σ uncertainties, where σ is the photometric rms noise. Uncertainties resulting from background subtraction are not shown. (The α Ori data have been excised from the λ Ori field spectral energy distribution.)

observed thermal dust luminosity (again see Table 3). For such an obscured cluster to exist, 99% of its luminosity must leak away, requiring it to be about ~ 40 pc on the far side of the Orion A cloud and unshrouded by dust or gas. Having $3.0 \times 10^7\ L_\odot$ of stellar luminosity, equivalent to a few dozen O stars, unfettered by dust and directly behind the Orion Nebula is a highly contrived situation, particularly when considering that a similar scenario would apply to NGC 2024. Hence, it is much more likely that hot dust emission is contributing substantially to the 4.9 μm band, especially in view of the observed 3.5 μm excess.

We can put upper limits on the mass of very hot ($T \geq 1000$ K) thermal equilibrium dust grains that are contributing to the near-IR by fitting modified blackbodies [i.e., of the form $\nu^\beta\ B_\nu(T)$, assuming $\beta = 2.0$ for the moment] to the entire DIRBE spectral range. In the Orion Nebula field, this limit is $\sim 10^{-11}$ of the mass or about $10^{-7}\ M_\odot$ of hot dust and associated gas, which is of the order of a few *lunar* masses. This upper limit is extremely sensitive to the value chosen for the dust emissivity index, β, but even using $\beta = 0.0$ gives an upper limit less than 1 $M_\odot$ for the hot thermal equilibrium dust and its associated gas. Given that the mass of ionized hydrogen in the Orion Nebula is $\sim 10\ M_\odot$ (see Balick 1974), this hot dust would be deeply embedded in the Orion Nebula itself. If we consider those smaller stochastically heated grains (sizes = few Å) that reach, or exceed, temperatures of 1000 K for a tiny fraction of the time, these grains and their associated gas comprise roughly 10^{-3} of the total mass, or $\sim 4\ M_\odot$, within the beam centered on the Orion Nebula (E. Dwek, private communication). Therefore, it is very likely that dust grains that achieve temperatures at, or exceeding, 1000 K, if only for part of the time, are only a negligible fraction of the dust mass on the very large size scales considered in this paper; although it is still possible that such hot, or temporarily hot, grains make a nonnegligible contribution to the observed near-IR emission.

At the other end of the spectrum, the 100 μm, 140 μm, and 240 μm fluxes provide crude estimates of both the dust temperature for the big grains ($\gtrsim 0.01$ μm), $T_{\rm dust}$, and a spectral emissivity index, β (for a ν_β emissivity law). Fitting the fluxes for the entire region (Orion A + Orion B + λ Ori fields) results in $T_{\rm dust} \simeq 20$ K and $\beta \simeq 2.0$ These results are rather uncertain because the 100 μm band has a different calibrator than the 140 and 240 μm bands. Using the *COBE*/Far-Infrared Absolute Spectrophotometer (FIRAS) data covering wavelengths 104–2000 μm and covering positions corresponding to the large fields does not uniquely constrain the spectral emissivity index. Fits with the emissivity index, β, fixed at 2.0 are nearly as good as, or better than, fits where β is varied. Even when β is varied for the Orion B and λ Ori fields, the best fits are still consistent with $\beta = 2.0$, within the uncertainties. For the Orion A field, the FIRAS data suggest $\beta = 1.4 \pm 0.1$, but assuming two distinct temperature components with β fixed at 2.0 yields a fit that is just as good. Therefore, we will adopt an emissivity law of $\beta \equiv 2.0$. Additional reasons for using $\beta = 2.0$ are as follows.

1. The optical depth to gas column density ratio, $\tau(100\ \mu\text{m})/N(\text{H I} + 2\text{H}_2)$, is consistent with that of Draine & Lee (1984) when the dust-derived column density, $N(\text{H})_{\rm dust}$, is computed using $\beta = 2$ (see § 3.3.2).

2. Big grains are expected to have $\beta = 2$ (Andriesse 1974; Seki & Yamamoto 1980).

Adopting $\beta = 2.0$ gives an $I_\nu(100\ \mu\text{m})/I_\nu(240\ \mu\text{m})$ color temperature within ~ 2 K of that of $I_\nu(140\ \mu\text{m})/I_\nu(240\ \mu\text{m})$.

Variations in the shapes of the spectral distributions as a function of radius are illustrated in the surface plots in Figures 6*a*–6*c*. Each slice in radius represents the spectral distribution averaged over an annulus 0.°35 wide and centered on the Orion Nebula (Fig. 6*a*), NGC 2024 (Fig. 6*b*), and the star λ Ori (Fig. 6*c*). For the Orion Nebula, notice that as the near-IR intensities decline by a factor of ~ 4 at a radius of ~ 12–15 pc, the far-IR peak shifts from 60 μm to 140 μm ($\log \nu = 12.70$–12.33). At a similar radius, $r \simeq 10$ pc, the 3.5 μm ($\log \nu = 13.93$) excess disappears. At a radius exceeding 20 pc, the spectral distribution resembles that of the Galactic plane shown in Figure 5. Similar trends are apparent in the NGC 2024 annular spectral distributions, except that the far-IR peak starts near 100 μm ($\log \nu = 12.48$) before shifting to 140 μm ($\log \nu = 12.33$). The λ Ori annular spectral distributions go negative at 12 μm ($\log \nu = 13.40$) at intermediate radii (depicted as the "hole" in Fig. 6*c*) because of background oversubtraction in part of the λ Ori field at 12 μm. Zhang et al. (1989) had a similar problem with background subtraction; cuts through their 12 μm *IRAS* map of the λ Ori ring show negative intensities. In contrast with the Orion Nebula and NGC 2024 spectral distributions, the λ Ori spectral distribution resembles that of the Galactic plane (see Fig. 5) at all radii (except for $r \simeq 10$–16 pc, where the hole prevents the comparison).

3.3. *Temperatures and Column Densities*

All the temperatures and column densities discussed here, unless otherwise noted, are derived from the 140 μm and 240 μm intensities, which are largely free of contributions by small stochastically heated grains (Désert, Boulanger, & Puget 1990; Sodroski et al. 1994). Therefore, the 140 and 240 μm intensities give the temperatures and column densities of the large grains ($\gtrsim 0.01$ μm), which dominate the mass of the dust (Mathis, Rumpl, & Nordsieck 1977). The large grain temperature, $T_{\rm dust}$, is determined from

$$\frac{I_{\nu 9}}{I_{\nu 10}} = \frac{\nu_9^\beta\, B_{\nu 9}(T_{\rm dust}) K_{\nu 9}(T_{\rm dust}, \beta)}{\nu_{10}^\beta\, B_{\nu 10}(T_{\rm dust}) K_{\nu 10}(T_{\rm dust}, \beta)}, \tag{3}$$

where ν_9 is the frequency at $\lambda_9 = 140$ μm, ν_{10} is the frequency at $\lambda_{10} = 240$ μm, $I_{\nu 9}$ and $I_{\nu 10}$ are the quoted DIRBE intensities at frequencies ν_9 and ν_{10}, $B_\nu(T_{\rm dust})$ is the Planck function, K_ν is the DIRBE band color correction (usually $K_\nu \simeq 1$ for these observations of Orion, but this correction is necessary since $\Delta\nu/\nu$ is not negligible) and $\beta = 2.0$ is the adopted emissivity index (see previous section). The gas column densities inferred from dust emission, $N(\text{H})_{\rm dust}$, are then derived from the 240 μm optical depth, $\tau_{\nu 10} = I_{\nu 10}/[B_{\nu 10}(T_{\rm dust}) K_{\nu 10}(T_{\rm dust}, \beta)]$, assuming a 100 μm mass opacity, κ_{100}, of 40 cm^2 g^{-1} (E. Dwek, private communication), which corresponds to $\kappa_{240} = 6.9$ cm^2 g^{-1}, and a dust-to-gas mass ratio of 0.01. This is equivalent to $\tau(100\ \mu\text{m})/N(\text{H}) = 7 \times 10^{25}$ cm^2 (see Draine & Lee 1984). Given the 6% relative uncertainty between the 140 and 240 μm bands and their 11%–12% absolute uncertainty, we find that $T_{\rm dust}$ is accurate to $\pm 2\%$–5% and the masses and column densities are accurate to $\pm 20\%$–30% (for the adopted emissivity index and adopted gas-to-dust ratio).

The temperature and column density maps are shown in Figures 7 and 8. The temperature map shows that temperatures of 18 K, consistent with heating by the general interstellar radiation field (Désert et al. 1990), are most common over the large fields (i.e., Orion A, Orion B, and λ Ori), but within the H II regions, the Orion Nebula and NGC 2024, the

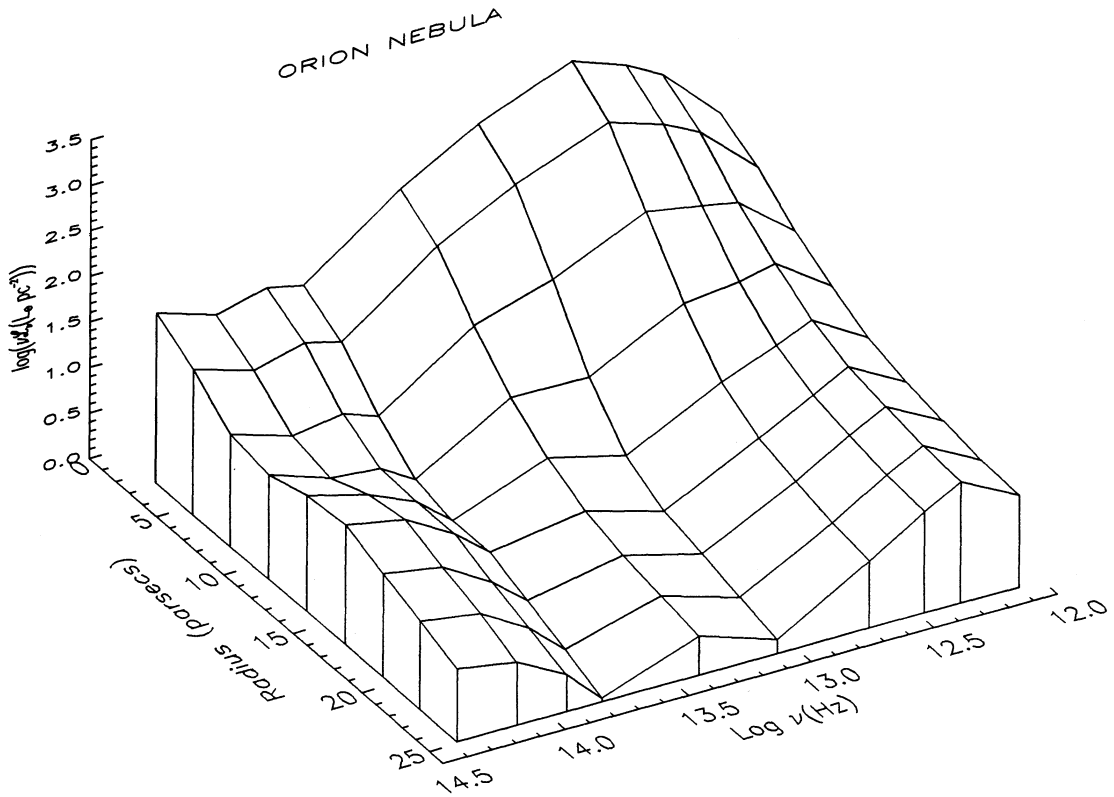

FIG. 6*a*

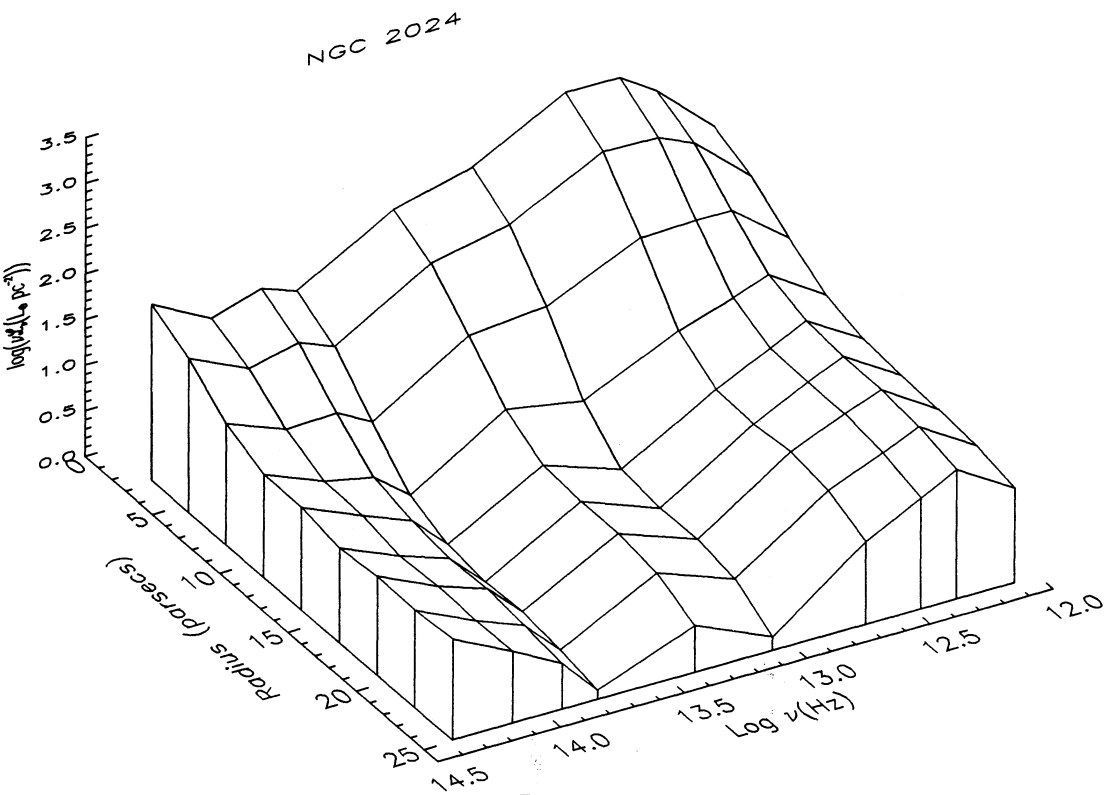

FIG. 6*b*

FIG. 6.—Radial variations in spectral energy distributions are displayed as surface luminosity, νL_ν, vs. radius and log (ν). Each slice at fixed radius represents the surface luminosity averaged over an annulus 0°.35 (2.7 pc) thick. The annuli are centered on (*a*) the Orion Nebula, (*b*) NGC 2024, and (*c*) the star λ Ori. A surface luminosity νL_ν of 1 $L_\odot$ pc^{-2} corresponds to a surface brightness, νL_ν, of 32 nW m^{-2} sr^{-1}. (The Orion Nebula data were excised from the NGC 2024 spectral energy distributions, and vice versa, and the α Ori data were excised from the λ Ori spectral energy distributions.)

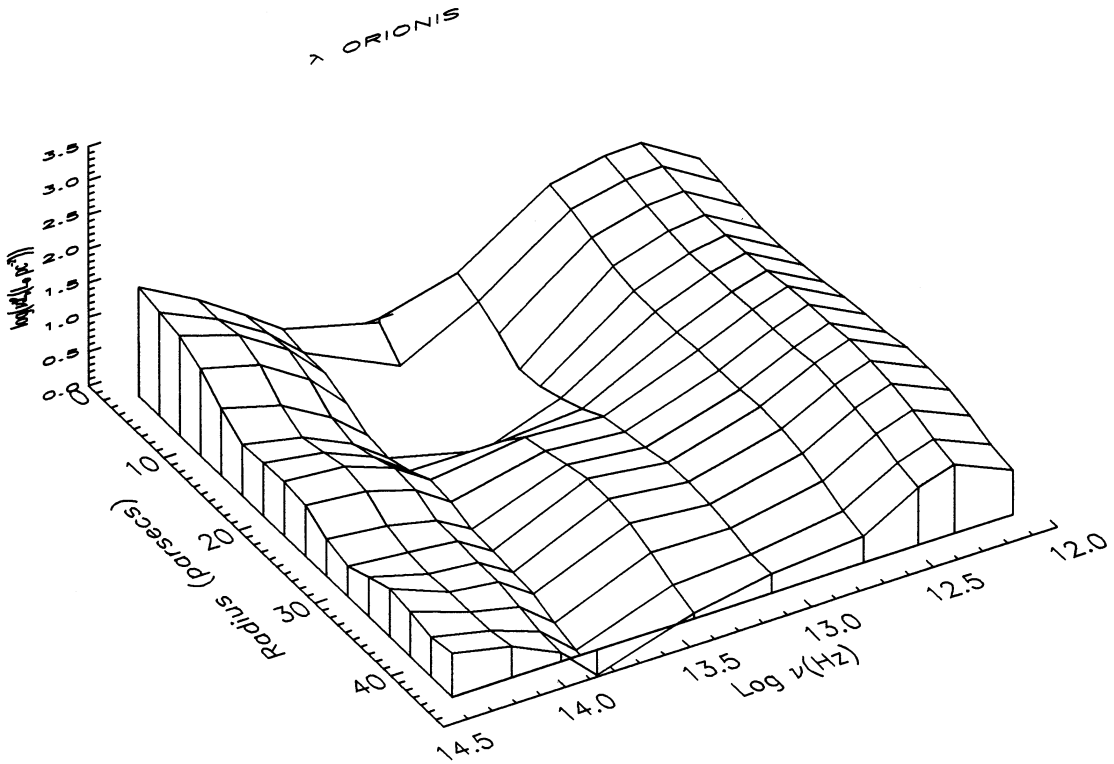

FIG. 6c

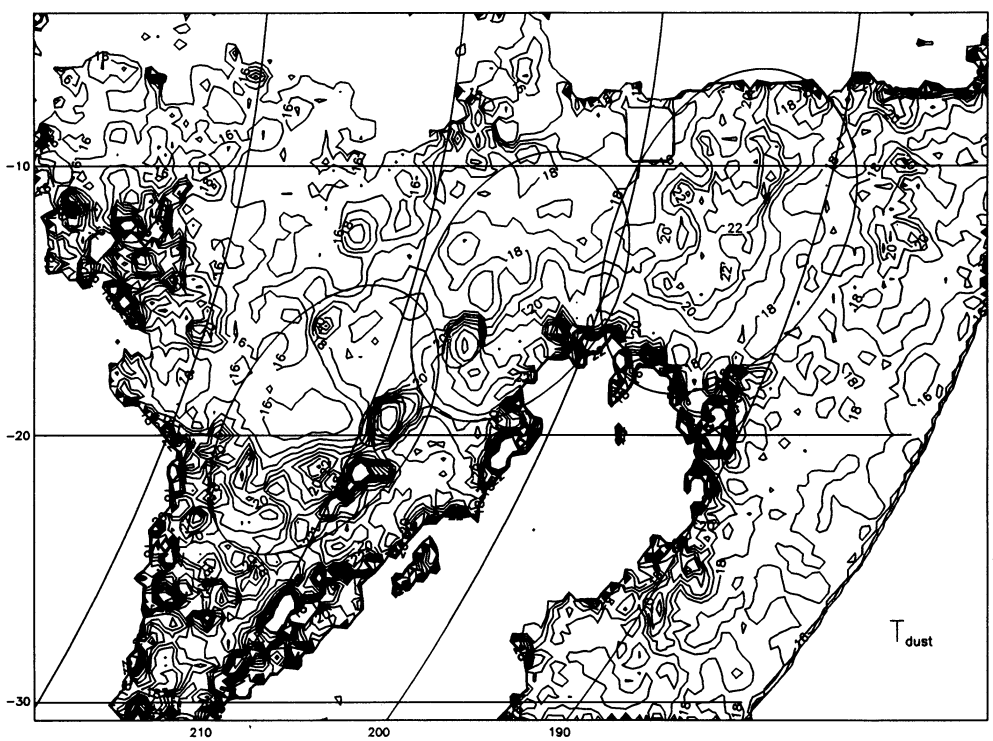

FIG. 7.—Spatial distribution of the 140 μm/240 μm color temperature, T_{dust}, is illustrated ($\beta = 2$ emissivity index unless otherwise stated). Contour levels are 15, 16, 17, ..., 30 K. For details, see § 3.3. All positions in the T_{dust} map where $I_\nu(140\ \mu m) < 1$ MJy sr^{-1} or $I_\nu(240\ \mu m) < 1$ MJy sr^{-1} were set to zero, resulting in the close spacing of contours at the edges of the emitting regions. The uncertainly in the derived color temperatures ranges from 2% for color temperatures of 15 K to 5% for color temperatures of 30 K. (The α Ori data were excised from the λ Ori field.)

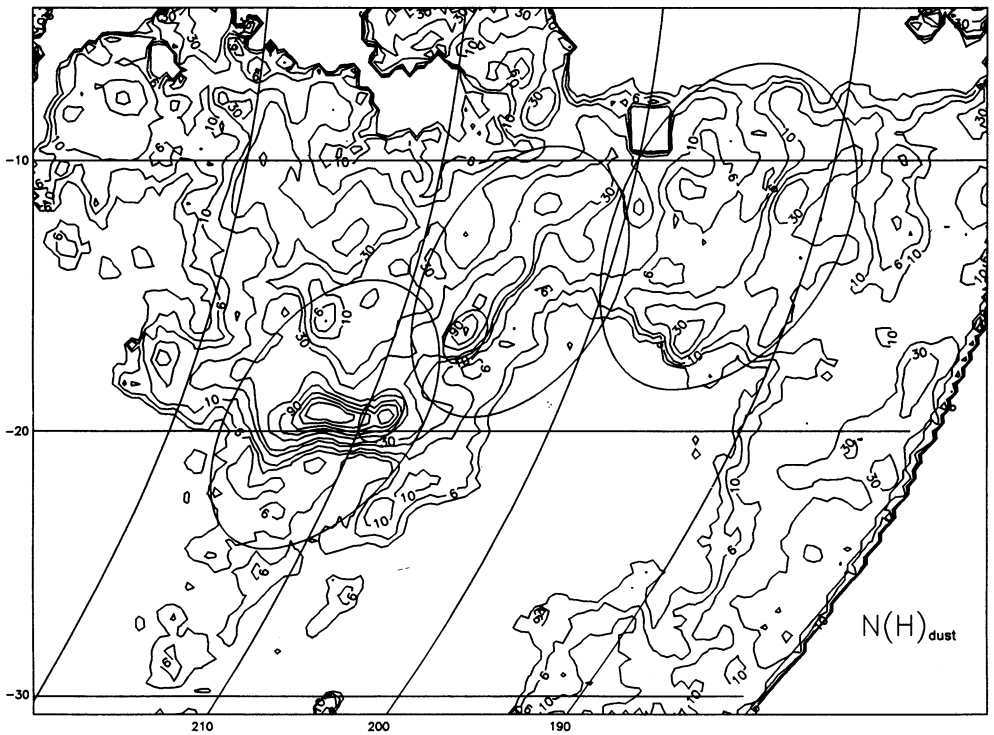

FIG. 8.—A map of dust-inferred gas column densities, $N(H)_{dust}$, is shown. These column densities were 140 and 240 μm intensities along with an assumed gas-to-dust ratio. Contour levels are 3, 6, 10, 20, 30, 60, 90, 120, 150, and 180 $\times 10^{20}$ H nuclei cm^{-2}. Uncertainties in the column densities due to the calibration uncertainties are 20%–30%. See § 3.3 for details. (The α Ori data were excised from the λ Ori field.)

temperatures are 25–26 K. The H II region inside the λ Ori dust ring has temperatures of $\sim$22 K. The Orion A cloud east of the Orion Nebula shows temperatures colder than 18 K, implying shielding from the GISRF and relatively few embedded stars. The possibility of strong shielding is supported by the high continuum densities ($> 10^{22}$ cm^{-2}) revealed in the column density map (Fig. 8) in the eastern tongue of the Orion A cloud. Similarly, the CO $J = 1 \rightarrow 0$ intensities (Fig. 3*a*) of the tongue imply column densities in excess of $\sim 5 \times 10^{21}$ cm^{-2}. The column density map also shows that the Orion Nebula and NGC 2024 are regions of enhanced column density as well as enhanced temperature. Further west, portions of the λ Ori dust ring—B30, B223, and Lynds 1602/3—are visible as column density enhancements [with $N(H)_{dust} \simeq 3 \times 10^{21}$ cm^{-2}] exterior to the area of temperature enhancement (with $T_{dust} \simeq$ 22 K).

A plot of dust temperature versus column density (Figs. 9*a*–9*b*) shows two distinct populations of points: those with an inverse temperature–column density correlation and those with highly scattered but possibly weak positive temperature correlation. Subjecting the two populations to the Kolmogorov-Smirnov test gives a better than 99% confidence in the *rejection* of the null hypothesis that the two populations are drawn from the same population. The former population is expected for externally heated clouds (i.e., few embedded heating sources), since a higher column density implies more shielding and, consequently, a lower temperature. The latter population occurs primarily in the Orion Nebula and NGC 2024 fields; because these fields have embedded stars, they are not expected to have the inverse temperature–column density correlation. The apparently positive temperature–column density correlation may suggest an increasing luminosity per unit gas mass with increasing gas mass. On the other hand, if one ignores the cluster of points at high temperatures ($T_{dust} >$ 25 K) and high column density [$N(H)_{dust} > 1.50 \times 10^{22}$ cm^{-2}], the "correlation" seems much flatter.

3.3.1. *Comparisons with Previous Studies*

Owing to the availability of *IRAS* data, dust column densities over the last decade have been estimated largely from 60 μm and 100 μm intensities. Since stochastically heated small grains ($\lesssim$0.01 μm) contribute substantially to 60 μm emission, the I_ν(60 μm)/I_ν(100 μm) ratio overestimates the large grain temperatures, yielding underestimated column densities. These column density underestimates are illustrated in Figures 10*a* and 10*b*, which show variations of the ratio of column densities estimated from the DIRBE 60 and 100 μm intensities, N(60 μm/100 μm), to that estimated from 140 and 240 μm intensities, $N(H)_{dust}$. The 60 and 100 μm intensities underestimate column densities by a factor of $\sim$5 in the warmer Orion Nebula and NGC 2024 field and by a factor of $\sim$10 elsewhere. Regions with higher temperature big grains give higher N(60 μm/100 μm)/$N(H)_{dust}$, which is clearly visible in the plot of N(60 μm/100 μm)/$N(H)_{dust}$ (see Fig. 10*a*). Note in Figure 10*b* that a $\beta = 1$ emissivity law would give N(60 μm/100 μm)/$N(H)_{dust}$ approaching unity in the high-temperature ($T_{dust} \simeq 30$ K) limit. Such was concluded by Bally et al. (1991) in their large-scale study of Orion's dust and gas using *IRAS* data; as the large grains became warmer, their contributions to the 60 μm emission increases relative to that of the stochastically heated small grains, providing progressively less drastic temperature overestimates of these large grains.

Even though the disagreement between 60/100 μm and 140/240 μm color temperatures (see Fig. 10*c*) is probably the

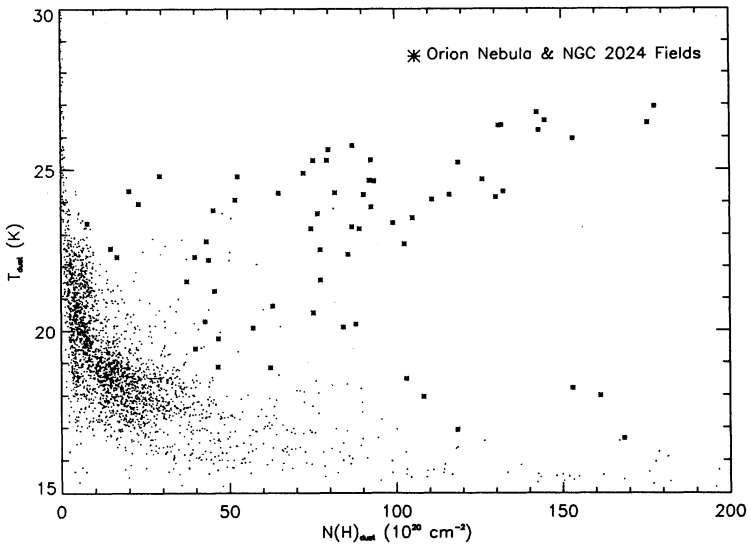

FIG. 9*a*

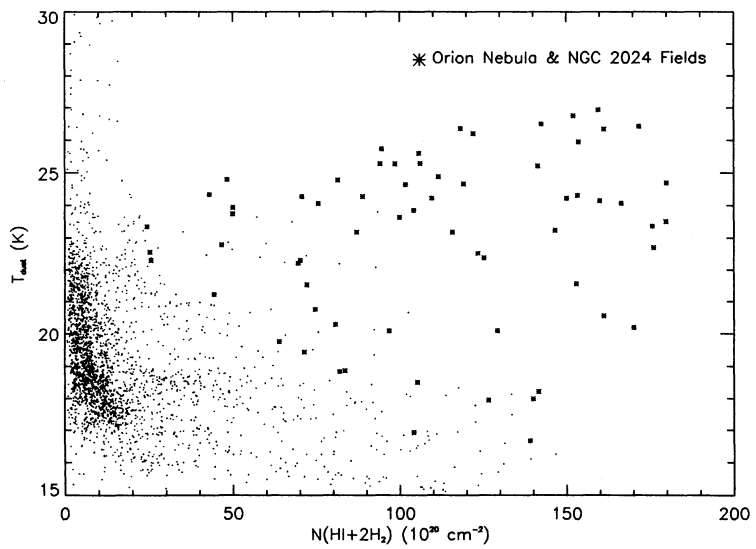

FIG. 9*b*

FIG. 9.—(*a*) A plot of T_{dust} vs. $N(H)_{dust}$ for positions within the Orion fields is shown. Asterisks represent positions within the Orion Nebula and NGC 2024 fields. (*b*) A plot of T_{dust} vs. $N(H\,I + 2H_2)$ positions within the Orion fields is shown. Asterisks represent positions within the Orion Nebula and NGC 2024 fields.

result of emission from stochastically heated dust grains contributing to the 60 μm band, other explanations based on these observed color temperatures are possible. If we assume grains at equilibrium, but with a distribution of temperatures, we can account crudely for the overall variation of $T(60/100\ \mu m)$ with $T(140/240\ \mu m)$ (also known as T_{dust}). Figure 10*c* shows a plot of the observed color temperatures along with two theoretical curves. The solid curve represents a sequence of exponentially weighted distributions of grain temperatures, where each distribution in the sequence has progressively more weight on the higher temperatures. Each distribution in the sequence has a lower temperature limit of 11 K and an upper limit of 100 K. The dashed curve represents the case of two distinct temperature components (15 K and 27 K) where again the weight on the higher temperature is progressively increased. The solid curve roughly follows the trend apparent in the H II region fields, whereas the dashed curve follows the trend outside the H II region fields.

Results of tests of the Boulanger et al. (1988) model by Bally et al. (1991) agree with those using DIRBE data. The model of Boulanger et al. (1988) predicts $I_\nu(60\ \mu m)/I_\nu(100\ \mu m)$ as a function of large-grain temperature, while taking stochastically heated grains into account. The Boulanger et al. model curve is plotted as a solid line in Figure 11 (in the manner of Bally et al. 1991) and has two values of T_{dust} for each value $I_\nu(60\ \mu m)/I_\nu(100\ \mu m)$. The high-temperature arm of the curve represents $I_\nu(25\ \mu m)/I_\nu(60\ \mu m) < 0.45$, and the lower-temperature arm represents $I_\nu(25\ \mu m)/I_\nu(60\ \mu m) > 0.45$. Dust emission on the low-temperature arm is dominated by emission from the stochastically heated grains, and dust emission on the high-temperature arm is dominated by emission from grains in thermal equilibrium. One would then expect, for

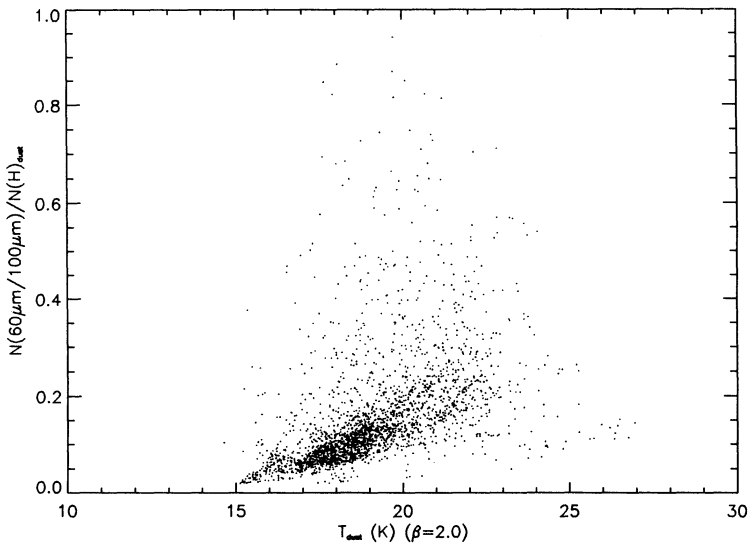

FIG. 10*a*

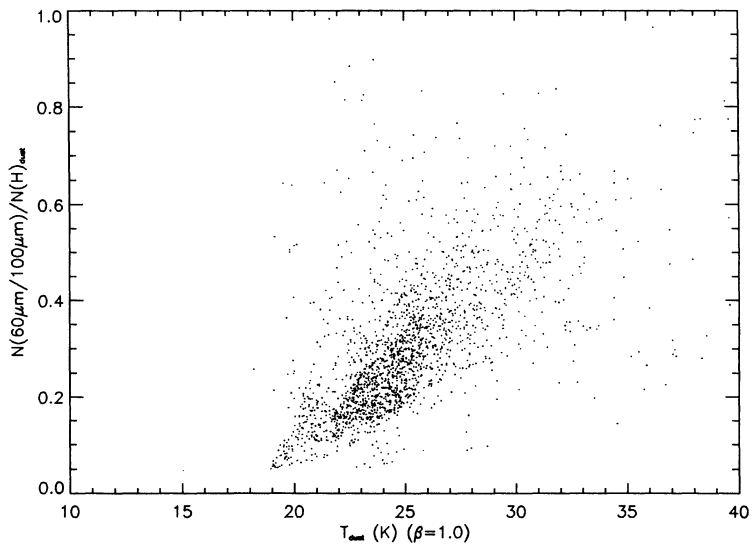

FIG. 10*b*

FIG. 10.—(*a*) A plot of the column density ratio $N(60\ \mu m/100\ \mu m)/N(H)_{dust}$ vs. T_{dust} is displayed for the usual $\beta = 2$ emissivity law. Plotted points represent positions inside the Orion Fields. Uncertainties in $N(60\ \mu m/100\ \mu m)$ attributable to the calibration uncertainties are 30%–50%. (*b*) A plot of the column density ratio $N(60\ \mu m/100\ \mu m)/N(H)_{dust}$ vs. T_{dust} is displayed for a $\beta = 1$ emissivity law. Plotted points represent positions inside the Orion fields. (*c*) A plot of the 60/100 μm color temperature, $T(60\ \mu m/100\ \mu m)$, vs. the 140/240 μm color temperature, T_{dust}, is shown, assuming $\beta = 2.0$ for both temperatures. The solid curve represents a sequence of exponentially weighted distributions of grain temperatures (lower temperature limit of 11 K and upper temperature limit of 100 K for each distribution), where each distribution in the sequence has progressively more weight on the higher temperatures. The dashed curve represents the case of two distinct temperature components (15 K and 27 K), where the ranges of the observed color temperatures are generated by progressively increasing the weight on the higher temperature component. Uncertainties in $T(60\ \mu m/100\ \mu m)$ due to the calibration uncertainties are 3.3%–6%.

example, dust grains in H II regions to follow the high-temperature arm because the grains in thermal equilibrium are warmer in H II regions than in the surrounding molecular gas and the emission from these grains will surpass the emission from stochastically heated grains. Data points in Figure 11 (where we assumed $\beta = 1$ in deriving T_{dust} to allow a valid comparison with Boulanger et al. 1988 and Bally et al. 1991) clearly show that points expected to be on the low-temperature arm [i.e., $I_\nu(25\ \mu m)/I_\nu(60\ \mu m) > 0.45$] are clustered on a section of the high-temperature arm and the rest are widely scattered about the high-temperature arm. Apparently, positions with large contributions from stochastically heated grain emission are characterized by roughly constant $I_\nu(60\ \mu m)/I_\nu(100\ \mu m)$ and roughly constant T_{dust} ($\sim$23 K for $\beta = 1$ or $\sim$18 K for $\beta = 2$), rather than following the low-temperature arm of the Boulanger et al. (1988) curve. This is also the conclusion of Bally et al. (1991), who were able to generate $\tau(100\ \mu m)$ maps in reasonable agreement with $^{13}CO\ J = 1 \rightarrow 0$ maps by assuming that positions with large proportions of emission in the mid-IR were at constant temperature.

Dust luminosities per unit gas mass for the different fields (see Tables 3 and 4), range from 2 $L_\odot\ M_\odot^{-1}$ for the λ Ori field to 20 $L_\odot\ M_\odot^{-1}$. The value for the combined fields is 3 $L_\odot\ M_\odot^{-1}$, which is comparable to a recent determination of far-IR lumi-

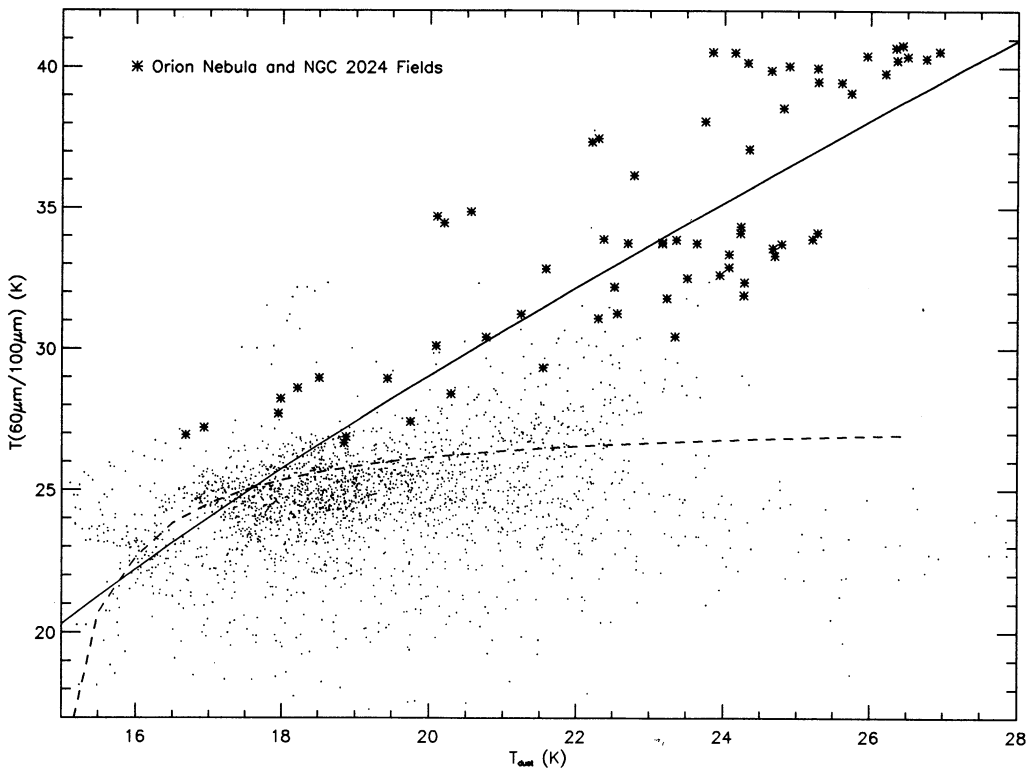

FIG. 10*c*

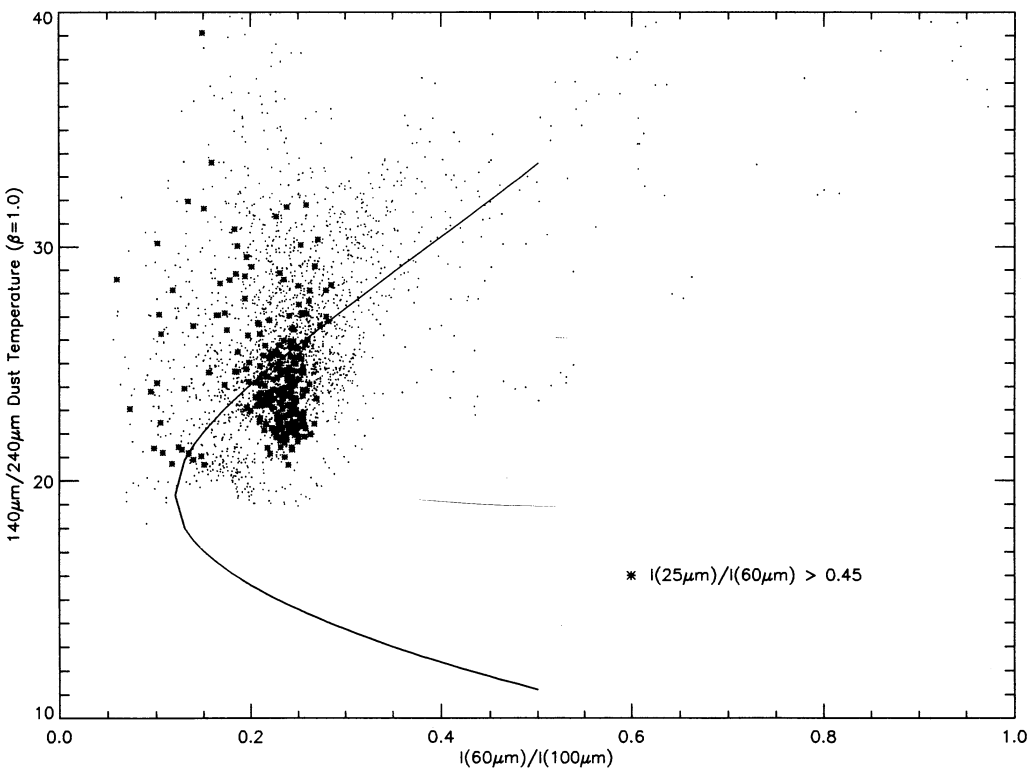

FIG. 11.—The 140 μm/240 μm color temperature for a $\beta = 1$ emissivity law is plotted against the $I_\nu(60\ \mu\text{m})/I_\nu(100\ \mu\text{m})$ intensity ratio. Asterisks represent positions at which $I_\nu(25\ \mu\text{m})/I_\nu(60\ \mu\text{m}) > 0.45$. The solid curve is from a model by Boulanger et al. (1988; see also Bally et al. 1991). Plotted points represent positions inside the Orion fields.

TABLE 4

MASSES OF ORION FIELDS

PHASE	MASS ($M_\odot$)					
	Orion Nebula	Orion A	NGC 2024	Orion B	λ Ori	Combined[a]
$M(\mathrm{H})_{\mathrm{dust}}$[b]	1.8×10^4	1.3×10^5	1.1×10^4	9.4×10^4	6.8×10^4	2.9×10^5
$M(\mathrm{H_2})$[c] + $M(\mathrm{H\ I})$[d]	1.9×10^4	1.2×10^5	1.7×10^4	1.0×10^5	4.5×10^4	2.7×10^5
$M(\mathrm{H_2})$[c]	1.7×10^4	9.8×10^4	1.6×10^4	8.3×10^4	2.7×10^4	2.1×10^5
$M(\mathrm{H\ I})$[d]	1.4×10^3	2.3×10^4	1.2×10^3	2.1×10^4	1.8×10^4	5.9×10^4

[a] Combined Orion A + Orion B + λ Ori field.
[b] Inferred from 140 and 240 μm fluxes and an assumed gas-to-dust ratio of 100; uncertainty of $\pm 20\%$–30%; see § 3.3.
[c] Using CO $J = 1 \rightarrow 0$ data of Dame et al. 1987; see §§ 2.2 and 3.3.
[d] Using H I 21 cm data of Heiles & Habing 1974; see §§ 2.2 and 3.3.

nosities per unit gas mass on a Galactic scale (i.e., 2–4 $L_\odot\ M_\odot^{-1}$ from Sodroski et al. 1994).

3.3.2. *Dust-to-Gas*

Comparing the column densities derived from 140 μm and 240 μm dust emission, $N(\mathrm{H})_{\mathrm{dust}}$, with those derived from gas, $N(\mathrm{H\ I} + 2\mathrm{H_2})$ (see Figs. 12 and 13 and Table 4) leads to the following conclusions.

1. The dust opacity per unit gas column density, $\tau(100\ \mu\mathrm{m})/N(\mathrm{H\ I} + 2\mathrm{H_2})$, is constant from position to position to within a factor of ~ 2. This is equivalent to saying that the dust-to-gas mass ratio does not vary spatially by more than a factor of ~ 2, if the dust grain properties (e.g., κ, β) are constant throughout the Orion fields.
2. Obtaining a $\tau(100\ \mu\mathrm{m})/N(\mathrm{H\ I} + 2\mathrm{H_2})$ value consistent with that of Draine & Lee (1984) requires $\beta = 2$. Choosing $\beta = 1.5$ results in a $\tau(100\ \mu\mathrm{m})/N(\mathrm{H\ I} + 2\mathrm{H_2})$ value factors of 2–3 smaller than that of Draine & Lee (1984).

Support for item 1 above is seen in Figure 12, Table 4, and Figure 13. Support for item 2 above is illustrated in the contrast between Figures 13*b* and 13*c*. These points are elaborated upon below.

The results presented in Figure 12 and Table 4 suggest that $\tau(100\ \mu\mathrm{m})/N(\mathrm{H\ I} + 2\mathrm{H_2})$ is roughly constant from position to position. Figure 12 shows that column densities determined from 140 μm and 240 μm intensities $N(\mathrm{H})_{\mathrm{dust}}$ are reasonably consistent with those determined directly from the gas emission, $N(\mathrm{H\ I} + 2\mathrm{H_2})$. (Note that the ionized gas contributes less than 10% to the total gas mass. See, for example, Balick 1974; Reich 1978.) The resultant masses for the Orion fields are listed in Table 4. Table 4 shows that, from field to field, the masses determined from dust emission are remarkably consistent with those from gas emission, suggesting roughly constant $\tau(100\ \mu\mathrm{m})/N(\mathrm{H\ I} + 2\mathrm{H_2})$; i.e., the Draine & Lee (1984) value for the opacity per unit gas column density. The biggest discrepancy lies in the λ Ori field, where $M(\mathrm{H})_{\mathrm{dust}}/M(\mathrm{H\ I} + 2\mathrm{H_2}) = 1.5$. Even though we neglect the ionized gas in Table 4, and its mass is a sizable 6000 $M_\odot$ (e.g., see Zhang & Green 1991), this is not sufficient to account for the discrepancy between $M(\mathrm{H})_{\mathrm{dust}}$ and $M(\mathrm{H\ I} + 2\mathrm{H_2})$. The λ Ori field suffers the most confusion from Galactic plane emission and has the greatest uncertainty in the background subtraction. Estimates of the H I mass, for example, range from $5 \times 10^3\ M_\odot$ to $8 \times 10^4\ M_\odot$ (see Zhang & Green 1991, and discussion therein). Adopting a value between the extreme estimates, $M(\mathrm{H\ I}) = 3.5 \times 10^4\ M_\odot$, would resolve the discrepancy in the λ Ori field.

The extent to which the dust opacity per unit gas column density does vary is best illustrated in the histograms of Figure 13. The histogram in Figure 13 shows the distribution of the ratio $N(\mathrm{H})_{\mathrm{dust}}/N(\mathrm{H\ I} + 2\mathrm{H_2})$, where $N(\mathrm{H})_{\mathrm{dust}}/N(\mathrm{H\ I} + 2\mathrm{H_2}) = 1$ corresponds to $\tau(100\ \mu\mathrm{m})/N(\mathrm{H\ I} + 2\mathrm{H_2}) = 7 \times 10^{-25}\ \mathrm{cm}^{-2}$. Variations in $\tau(100\ \mu\mathrm{m})/N(\mathrm{H\ I} + 2\mathrm{H_2})$ could be due to variations in the dust-to-gas ratio or variations in the dust and gas properties. Also shown in Figure 13 are histograms for those pixels where $\mathrm{H_2}$ gas dominates, $[2m_{\mathrm{H}} N(\mathrm{H_2})] > 2[m_{\mathrm{H}} N(\mathrm{H\ II})]$, and where H I gas dominates, $[m_{\mathrm{H}} N(\mathrm{H\ I}) > 2[2m_{\mathrm{H}} N(\mathrm{H_2})]$. In Figure 13*a*, the histograms have mean values of $N(\mathrm{H})_{\mathrm{dust}}/N(\mathrm{H\ I} + 2\mathrm{H_2}) = 1.4 \pm 0.7$ but have values from about 0.2 to about 2.7. However, this large range might be an artifact of background subtraction; Figure 13*b* displays $N(\mathrm{H})_{\mathrm{dust}}/N(\mathrm{H\ I} + 2\mathrm{H_2})$ histograms for data with no background subtraction for both the IR data and gas data, where the mean $N(\mathrm{H})_{\mathrm{dust}}/N(\mathrm{H\ I} + 2\mathrm{H_2})$ is 0.9 ± 0.3, with a slightly narrower range. Hence, $\tau(100\ \mu\mathrm{m})/N(\mathrm{H\ I} + 2\mathrm{H_2}) \simeq 1$ to within a factor of 2.

That β must be near 2.0 in order to have $\tau(100\ \mu\mathrm{m})/N(\mathrm{H\ I} + 2\mathrm{H_2})$ consistent with that of Draine & Lee (1984) is demonstrated in the contrast between Figures 13*b* and 13*c*. Figure 13*c* demonstrates the effect of lowering the emissivity index from $\beta = 2$ to $\beta = 1.5$: $\tau(100\ \mu\mathrm{m})/N(\mathrm{H\ I} + 2\mathrm{H_2})$ drops by factors 2.5 to 3 below that of Draine & Lee (1984). Hence, it seems likely that $\beta = 2.0$ is a reasonable choice for Orion for $\lambda = 100$–$240\ \mu$m. Notice that the conclusions drawn from Figures 13*a*–13*c* are insensitive to the choice of the value for $N(\mathrm{H_2})/\int T_R(^{12}\mathrm{CO}\ J = 1 \rightarrow 0)\,dV$, since the histograms for the $\mathrm{H_2}$-dominant pixels have mean values similar to those for the H I–dominant pixels.

Figure 14 reveals a clear correlation of $N(\mathrm{H})_{\mathrm{dust}}/N(\mathrm{H\ I} + 2\mathrm{H_2})$ with T_{dust}. In Figure 14 we have only included the points of high column density $[N(\mathrm{H\ I} + 2\mathrm{H_2}) > 2 \times 10^{21}\ \mathrm{cm}^{-2}]$, since these points are least affected by systematic errors in the background subtraction. The observed temperature variation of $N(\mathrm{H})_{\mathrm{dust}}/N(\mathrm{H\ I} + 2\mathrm{H_2})$, for $T_{\mathrm{dust}} \gtrsim 19$ K, is probably not a real temperature dependence of the dust-to-gas ratio or of the dust and gas properties. Given the upsweep at $T_{\mathrm{dust}} \simeq$ 24–27 K, it is more likely that there is a temperature-dependent systematic error in the derivation of $N(\mathrm{H})_{\mathrm{dust}}$ for $T_{\mathrm{dust}} \gtrsim 19$ K. One assumption employed in the column density derivation is that of a single temperature along the line of sight. If, for simplicity, we postulate the existence of two distinct temperature components among the large grains, then our derivations assuming a single temperature would underestimate the true column density. An underestimate results because even a small contribution by warm dust to the overall column density will result in a significant overestimate of the

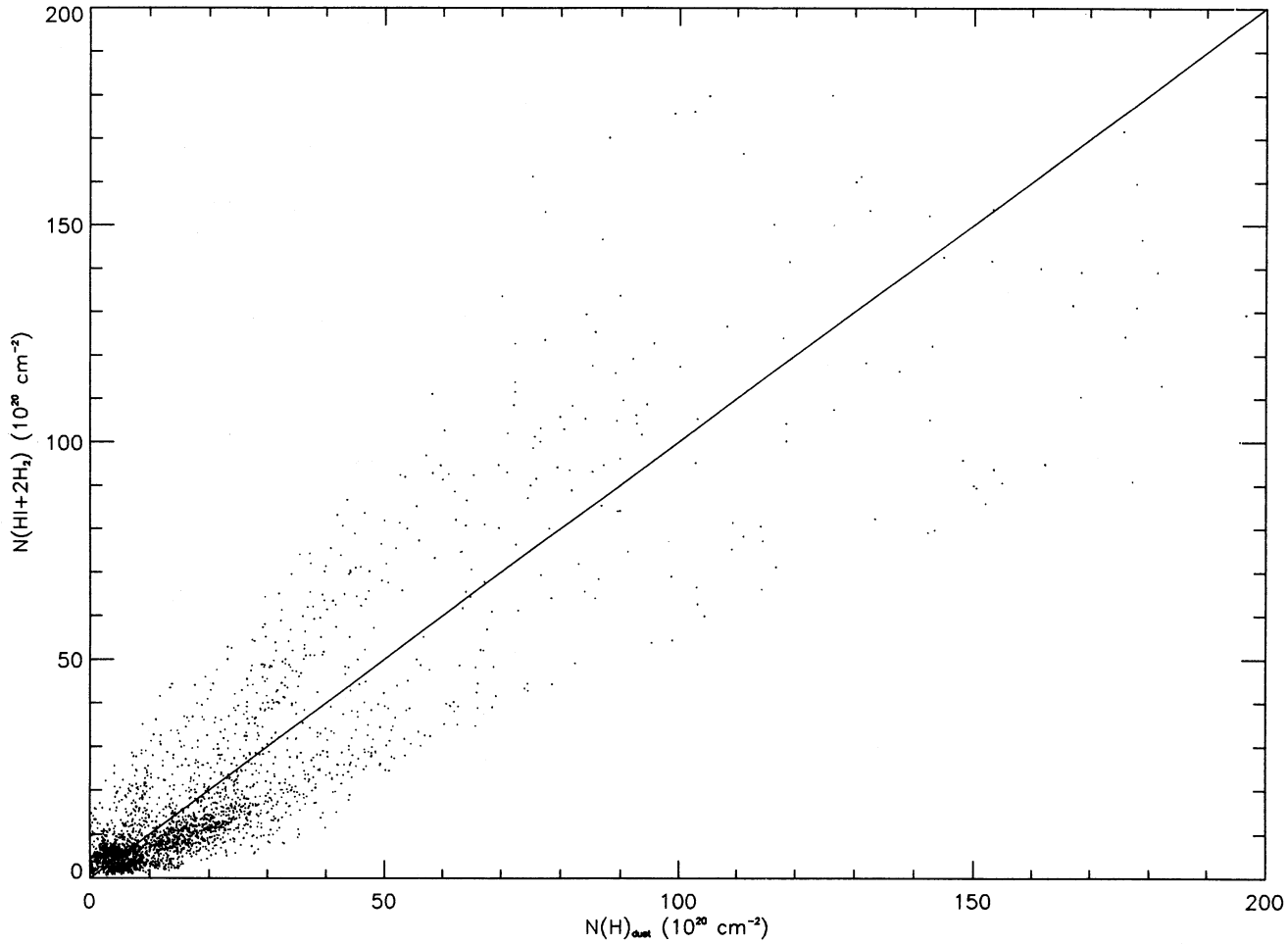

FIG. 12.—The gas column densities, $N(\mathrm{H\ I} + 2\mathrm{H}_2)$, are plotted against the dust-inferred gas column densities, $N(\mathrm{H})_{\mathrm{dust}}$, for positions within the Orion fields. A solid line with slope = 1 has been plotted for comparison.

temperature in the dominant cold component. The solid curve in Figure 14 illustrates the ratio of the inferred column density to the "corrected" total column density expected for dust consisting of a cold component with temperature 17 K and a warm component with a temperature of 27 K. The degree of $N(\mathrm{H})_{\mathrm{dust}}$ underestimation for color temperatures between 17 K and 27 K depicted by the curve, while roughly 50% too high, nevertheless follows the general trend in the data: underestimation is most pronounced at intermediate color temperatures and is least pronounced at the extreme (i.e., 17 and 27 K) color temperatures. For color temperatures less than 17 K, the theoretical curve also roughly reproduces the column density *overestimates*. This is accomplished by assuming that the cold component is itself composed of grains with two distinct spectral emissivity indices, 1.5 and 2.0, but only along lines of sight with no warm component. Hence, positions with no warm component may be heavily shielded from interstellar radiation (e.g., the eastern tongue of Orion A) and have grains with different properties, such as a lower spectral index, possibly due to the formation of amorphous mantles. It should be mentioned that explanations involving grain temperatures variation alone, i.e., constant emissivity index, cannot account for the steep decline of $N(\mathrm{H})_{\mathrm{dust}}/N(\mathrm{H\ I} + 2\mathrm{H}_2)$ with color temperature seen for color temperatures $\lesssim 18$ K, even if a higher value of the dust opacity per unit gas mass is chosen. Also notice that the continuous temperature distribution depicted by the solid curve in Figure 10*c*, to account for the variation of the 60/100 μm color temperature with 140/240 μm color temperature, is not needed when accounting for variation of $N(\mathrm{H})_{\mathrm{dust}}/N(\mathrm{H\ I} + 2\mathrm{H}_2)$ with 140/240 μm color temperature.

The above explanation for the trend of $N(\mathrm{H})_{\mathrm{dust}}/N(\mathrm{H\ I} + 2\mathrm{H}_2)$ with T_{dust} assumes that the gas column densities are themselves immune to systematic variations with the 140/240 μm color temperature. All the points of high column density used in this plot represent positions dominated by molecular gas. If the molecular gas temperature is correlated with dust temperature, then the fixed value of the $N(\mathrm{H}_2/\int T_R(^{12}\mathrm{CO}\ J = 1 \rightarrow 0)dV$ ratio used to estimate the molecular gas column density would yield a systematic variation in $N(\mathrm{H})_{\mathrm{dust}}/N(\mathrm{H\ I} + 2\mathrm{H}_2)$ with T_{dust}, since the $N(\mathrm{H}_2)/\int T_R(^{12}\mathrm{CO}\ J = 1 \rightarrow 0)dV$ ratio is actually temperature sensitive (e.g., see Maloney & Black 1988; Mead & Kutner 1988). However, it is difficult to see how gas properties alone could account for both the steep decline at $T_{\mathrm{dust}} \lesssim 18$ K *and* the upsweep at $T_{\mathrm{dust}} \simeq 24$–28 K.

3.4. *The Nature of the Excess in the DIRBE 3.5 μm Band—PAH 3.3 μm Line?*

Excess emission has been observed in the DIRBE 3.5 μm band relative to the emission in the adjacent bands, which could be caused by the 3.3 μm line of polycyclic aromatic

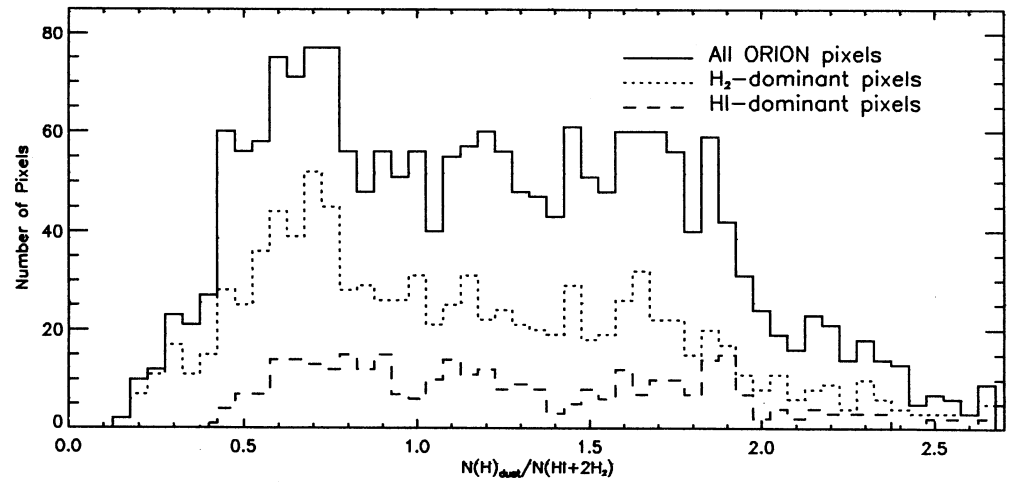

FIG. 13*a*

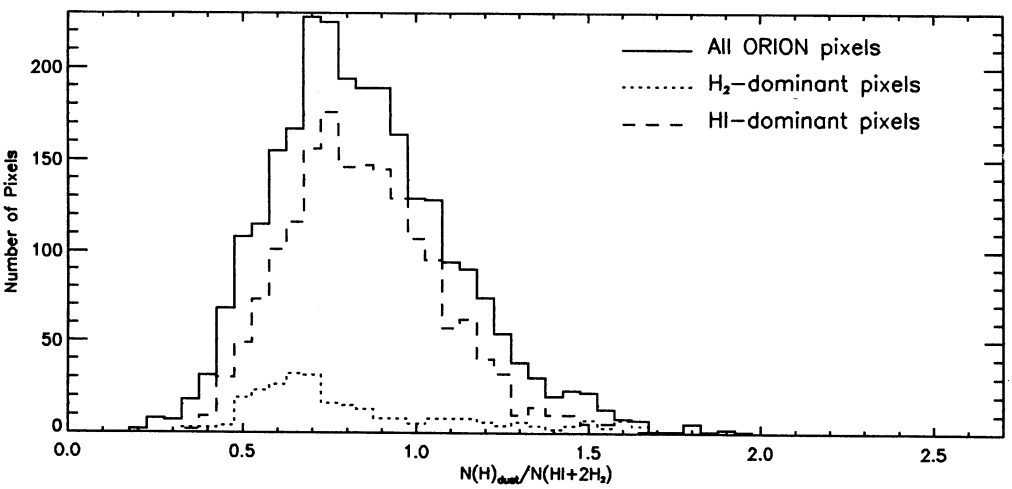

FIG. 13*b*

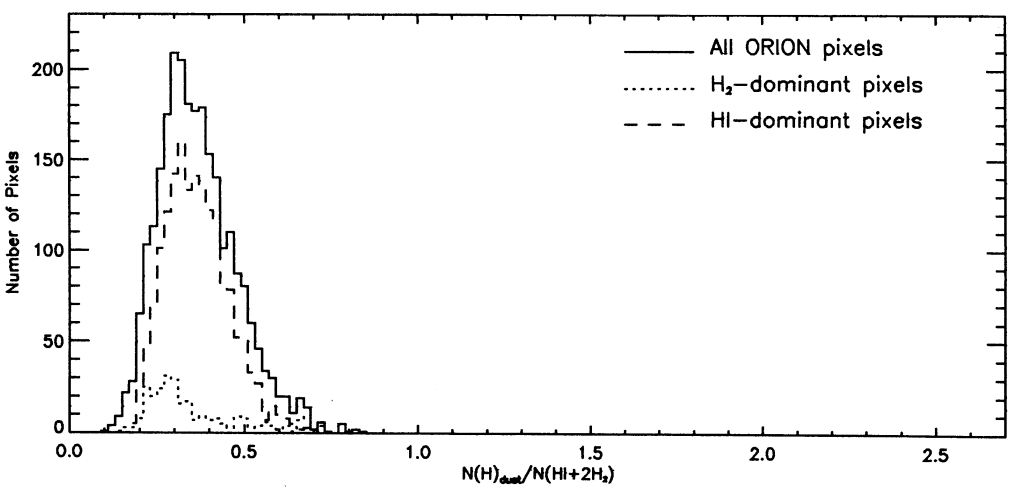

FIG. 13*c*

FIG. 13.—(*a*) A histogram of normalized dust-to-gas ratios $N(\mathrm{H})_{\mathrm{dust}}/N(\mathrm{H\ I} + 2\mathrm{H}_2)$ is presented for all positions in the Orion fields (*solid line*), for molecular gas dominant positions in the Orion fields (*dotted line*), and for atomic gas dominant positions within the Orion fields. A given pixel is considered to be dominant in molecular (or atomic) gas if the mass of molecular (or atomic) gas within the pixel is more than double that of the atomic (or molecular) gas. An emissivity index of 2.0 is assumed. (*b*) A histogram of $N(\mathrm{H})_{\mathrm{dust}}/N(\mathrm{H\ I} + 2\mathrm{H}_2)$ value is presented using data with *no background subtraction.* An emissivity index of 2.0 is assumed. (*c*) A histogram of $N(\mathrm{H})_{\mathrm{dust}}/N(\mathrm{H\ I} + 2\mathrm{H}_2)$ values is presented using data with *no background subtraction and a* $\beta = 1.5$ *emissivity law.*

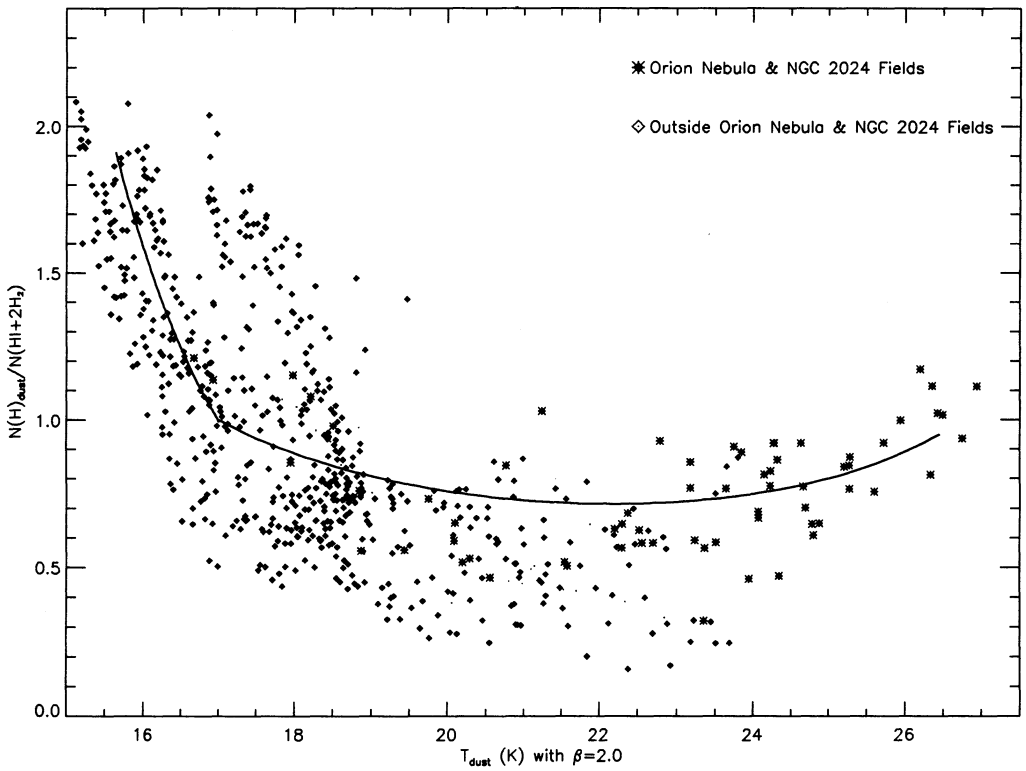

FIG. 14.—The normalized dust-to-gas ratio, $N(H)_{dust}/N(H\,I + 2H_2)$, is plotted against the 140/240 μm color temperature (for emissivity index = 2.0) for positions with high gas column density [$N(H)_{dust}/N(H\,I + 2H_2) > 2 \times 10^{21}$ cm^{-2}]. Solid curve represents the theoretically determined ratio of inferred-to-"true" dust column density values assuming two separate temperature components: a 17 K component and a 27 K component. The steep section of the curve at color temperatures less than 17 K makes the additional assumption that positions of low color temperature (i.e., < 17 K), contain grains with a mix of two distinct emissivity indices: 1.5 and 2.0. Note that all the points in this plot represent molecular gas dominant positions, including the positions inside the Orion Nebula and NGC 2024 fields.

hydrocarbons (see below). While the DIRBE instrument is unsuitable for detailed study of this line, we nevertheless present results that require confirmation by a narrow-band instrument.

PAHs were first suggested by Léger & Puget (1984) to account for several near-IR spectral features. PAHs absorb energetic (i.e., ultraviolet) stellar photons and emit in seven lines at $\lambda = 3.3$, 3.4, 6.2, 7.7, 8.6, 11.3, and 12.7 μm and in the near-IR to mid-IR continuum. Near- to mid-IR line emission by PAHs provide additional diagnostics for probing conditions in the ISM. While the 3.3 μm PAH line has been observed in H II regions and reflection nebulae, and even the external galaxies M82 and NGC 253 (e.g., see Sellgren 1981, and references therein; Mouri et al. 1990; Mizutani, Suto, & Maihara 1994; Mazzarella et al. 1994), large-scale maps of this feature had not existed until the AROME balloon experiment by Giard et al. (1989, 1994), which mapped the Galactic plane from $l = -60°$ to $+60°$ and $b = -5°$ to $+5°$. The AROME map shows knots, often lying toward known H II regions, enveloped in a smoother diffuse emission.

The 3.5 μm band excess relative to that from the 2.2 μm and 4.9 μm bands apparent in the Orion fields (see Fig. 5) is probably both 3.3 μm PAH line emission and hot dust continuum emission; indeed, the large $I_\nu(4.9\ \mu m)/I_\nu(1.25\ \mu m)$ ratio discussed in § 3.2 argues for the existence of hot dust continuum emission at near-IR wavelengths (note that a continuum-like "plateau" emission from PAH molecules is also possible in the 3.5 μm band along with much weaker emission lines; e.g., see Geballe et al. 1989). By comparing the excess observed in DIRBE's 3.5 μm band with the narrow-band observations of others (e.g., Sellgren 1981), we can estimate the proportion of the excess caused by the 3.3 μm PAH line. The 3.5 μm band excess map in Figure 15 is the difference between the 3.5 μm map and a map derived from the linear interpolation between the 2.2 and 4.9 μm maps in νL_ν units. Specifically, the interpolated 3 μm continuum map, $I_{\nu 3c}$, was estimated from

$$\nu_3 I_{\nu 3c} = \left(\frac{\nu_3 - \nu_2}{\nu_4 - \nu_2}\right)\nu_4 I_{\nu 4} + \left(\frac{\nu_4 - \nu_3}{\nu_4 - \nu_2}\right)\nu_2 I_{\nu 2}\,, \qquad (4)$$

where $I_{\nu 2}$ and $I_{\nu 4}$ are the 2.2 and 4.9 μm maps and ν_2, ν_3, and ν_4 are the frequencies corresponding to $\lambda = 2.2$, 3.5, and 4.9 μm, respectively. The map of the excess in-band brightness is then given by

$$I_{3x} = (I_{\nu 3} - I_{\nu 3c})\Delta\nu_3\,, \qquad (5)$$

where $I_{\nu 3}$ is the 3.5 μm map and $\Delta\nu_3$ is the bandpass for DIRBE's 3.5 μm band.

The linear interpolation between the 2.2 μm and 4.9 μm band intensities will overestimate the 3.3 μm continuum expected from stars by 2%–37% for a large range of stellar color temperatures (3000–50,000 K). An *overestimate* of the 3.3 μm continuum would imply an *underestimate* of the 3.3 μm PAH line, so false positive detections of the 3.3 μm PAH line occur only when the 3.3 μm continuum is underestimated by the interpolation. There are two cases in which the 3.3 μm continuum would be underestimated by the interpolation represented in equation (4). The first case occurs for hot dust

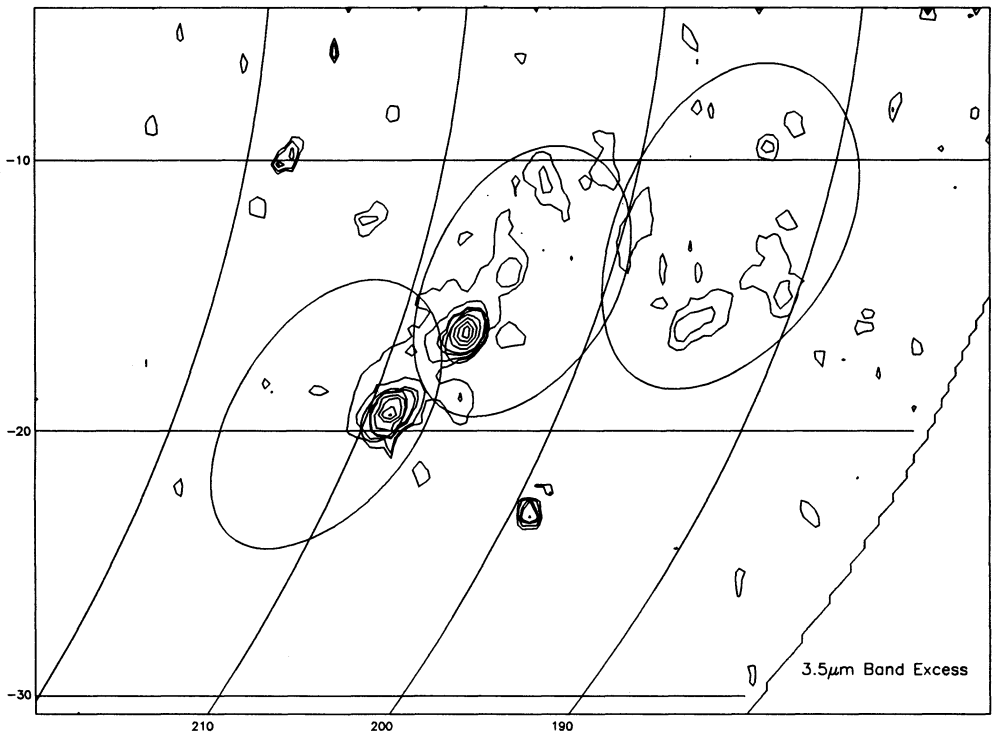

FIG. 15.—The spatial distribution of the excess in the DIRBE 3.5 μm band is illustrated. The contour levels are 0.2, 0.4, 0.8, 1, 2, 3, 4, and 5 $L_\odot$ pc^{-2}. A surface luminosity of 1 $L_\odot$ pc^{-2} is equivalent to a frequency-integrated surface brightness of 32 nW m^{-2} sr^{-1}.

continuum emission with a color temperature of ~1000 K, which would result in an underestimate of up to 20%. Indeed, the possible presence of such hot dust was discussed in § 3.2. Since the typical excess-to-continuum ratio in the Orion map is ~0.2–0.3, at least some of the 3.5 μm band excess could be caused by the PAH line. This is especially true in the H II region fields, where the excess-to-continuum ratio is 0.4, suggesting that at least $\frac{1}{3}$ of the excess may be caused by the PAH line. The second case occurs in the presence of appreciable extinction ($A_V \gtrsim 7$ mag, for a stellar temperature $\geq 10^4$ K). To place limits on the effects of extinction, we used the column densities derived from 140 and 240 μm intensities and the Rieke & Lebofsky (1985) reddening law to "correct" the 2.2, 3.5, and 4.9 μm maps, assuming that all the dust extinction is in the foreground. If this extinction correction changes the excess into a deficit at a given position, then it is likely that some or all of the original excess at that position was an artifact of the extinction and not caused by PAH line or hot dust continuum emission. *Indeed, it must be emphasized that a 3.5 μm band excess map of the Galactic plane failed this test. Hence, any DIRBE Galactic plane maps of the 3.5 μm band excess must be viewed with extreme caution.* For the Orion fields the excess *increased*, rather than decreased, after applying the extreme extinction correction, for all but the λ Ori field (which decreased by only 20%). The extinction correction, being extreme and used only as a test for artifacts, has not been included in the final map of the 3.5 μm excess.

Given that the 3.5 μm band excess is probably caused by a combination of hot dust continuum emission and PAH (line + plateau) emission, how much of this is from the 3.3 μm PAH line? Sellgren (1981) mapped a 6′ × 6′ region centered on the Orion Nebula in this PAH line. The total flux density in her map is about 450 Jy, or 23 Jy averaged over the DIRBE 3.5 μm band (width of 0.97 μm FWHM). The Orion Nebula flux density in the excess in the DIRBE 3.5 μm band is 80 Jy over a 40′ × 40′ area. The extra 57 Jy in the DIRBE map could be caused by low-level emission (~5% of the lowest contour in the Sellgren line map) outside the region mapped by Sellgren. At the very least, ~30% of the Orion Nebula 3.5 μm band excess observed by DIRBE is caused by 3.3 μm PAH line emission. Further determinations of the fraction of the DIRBE 3.5 μm band excess caused by the PAH 3.3 μm line can be carried out with the space-based observations of the Infrared Space Observatory (ISO; Kessler 1992) and the Infrared Telescope in Space (IRTS; Matsumoto 1993).

Contribution by lines other than the 3.3 μm PAH line to DIRBE's 3.5 μm band are negligible. Examination of spectra of H II regions and planetary nebulae in the range λ = 3.3–3.7 μm (Sellgren et al. 1990; Geballe et al. 1985) show no other strong spectral features. However, the DIRBE 3.5 μm band bandpass extends from 3.05 to 4.05 μm at the −10 dB points. Spectra of the BN object in the Orion Nebula covering the range 3.6–4.2 μm (Scoville et al. 1983) suggest that the only prominent lines are two recombination lines of hydrogen: Brα and Pfγ. The reduced response of the 3.5 μm band at 4.05 μm combined with observations of the Orion bar (Sellgren, Tokunaga, & Nakada 1990) implies that the Brα line's contribution to the 3.5 μm band is an order of magnitude lower than that of the 3.3 μm PAH line. The Pfγ line is down by another factor of ~2 (using the Scoville et al. 1983 data and the bandpass of the 3.5 μm band). Checking for contributions of lines in the 3.0–3.2 μm range to the DIRBE 3.5 μm band is problematic; the opacity of the Earth's atmosphere in this wavelength interval means that few if any spectra covering this range exist in the literature. If we assume that only hydrogen and helium lines are important, then only Pfε (λ = 3.04 μm) occurs in the ~3.0–3.2 μm interval

(note that Pfδ at $\lambda = 3.296$ μm would occur near the edge of the PAH 3.28 μm line). If this line is roughly as strong as Pfγ, then no lines other than the 3.3 μm PAH line contribute appreciably to DIRBE's 3.5 μm band.

If the 3.5 μm band excess is indeed caused by PAHs, then there should exist a correlation between the strength of this excess and the 12 μm emission, which is also believed to come partly from PAHs (see Désert et al. 1990). Such a correlation is demonstrated in Giard et al. (1989) and in Figure 16*a*. However, if this correlation is due only to PAH emission at 3 and 12 μm, then a correlation of the 3.5 μm band excess with 140 μm emission is not required, but indeed exists, as is demonstrated in Figure 16*b*. (Note that these correlations exist whether or not the Orion Nebula and NGC 2024 fields are included in the plots.) Therefore, this 3.5 μm band excess is possible wherever there is dust emission and is not necessarily correlated with carriers of lines in the DIRBE 12 μm band. If the 3.5 μm band excess is indeed caused by PAHs, then these correlations suggest that whenever there is dust there is PAH line emission.

We derive $I_{3.x}/\nu L_\nu(12\ \mu\text{m}) \simeq 0.03$, which is a factor of about 3 higher than the 3.3 μm PAH line to 12 μm intensity ratio obtained from the AROME and *IRAS* observations. This disagreement is easily explained if $\frac{2}{3}$ of the DIRBE excess is caused by hot dust continuum emission, in addition to the PAH line emission, which is consistent with the comparison with Sellgren (1981). Also, the disagreement could be the result of differences in the types of sources observed, since the AROME observations sample diffuse emission as well as compact sources—H II regions—whereas the DIRBE map of the 3.5 μm band excess samples mostly the H II regions. Another possible source of disagreement is that the AROME continuum map (from their channel B) is about 50% brighter than the DIRBE 3.5 μm continuum map. Since the DIRBE absolute calibration is good to 3%–4% at near-IR wavelengths, the AROME calibration could be in error. However, it could be argued that any comparison with the AROME data requires simulating the AROME observations (e.g., chopped observations with a throw of 1°.7 in right ascension) and the subsequent data reduction; even if their channel B calibration does not yield absolute intensities, the difference between channels A and B might possibly give correct PAH line intensities.

The luminosities in the 3.5 μm band excess for the Orion fields are listed in Table 3. The total 3.5 μm band excess luminosity is 2000 $L_\odot$, which is $\sim$0.2% of the 12–240 μm luminosity. This number is roughly comparable to that expected for the Galactic plane (crudely estimated from the AROME PAH line map and the DIRBE Galactic plane 12–240 μm data) and for external galaxies (Mouri et al. 1990).

4. ENERGY BUDGET: ORION STARS VERSUS GISRF

Here we estimate the fraction of the dust luminosity that is attributable to dust heated by the general interstellar radiation field (GISRF) and the fraction attributable to dust heated by the Orion stars. We assume that the GISRF has a constant energy density on scales of hundreds of parsecs (i.e., scales much larger than the Orion fields) and that the Orion stars provide a localized enhancement to the interstellar radiation field. For the GISRF, we adopt the value for the local interstellar radiation field determined by Mathis et al. (1983). We use their estimated wavelength-integrated mean intensity of $U_G \equiv \int_{0.09\ \mu\text{m}}^{8\ \mu\text{m}} 4\pi J_\lambda\, d\lambda = 2.2 \times 10^{-2}$ ergs s^{-1} cm^{-2}, which corresponds to 50 $L_\odot$ pc^{-2}.

4.1. *Maps of the Radiation Field*

Deriving a map of the radiation field strength in Orion requires detailed knowledge of the positions of the stars and dust in three dimensions, and detailed knowledge of their properties. Since precise depth perception is not possible, we are restricted to a simplified two-dimensional geometry. Using this simplified geometry and the positions and luminosities of the stars of Orion OB1 and λ Ori OB associations (Warren & Hesser 1977; Murdin & Penston 1977), we derived a map of the interstellar radiation field in Orion, with the following assumptions:

1. All the material is in a plane normal to the line of sight at a distance of 450 pc.
2. A few stars are offset, along the line of sight, from this plane to prevent singularitites in the radiation field derivation. Two standard distances for the offsets were chosen: 1 pc and 10 pc. The offset chosen for most stars is 1 pc, about half the DIRBE pixel size at the distance of Orion. The exact value for the offset most strongly affects the pixels containing stars, but only weakly affects the radiation field values on larger size scales. A few of the most luminous stars were given the larger offset of 10 pc to prevent the dust luminosity in their direction from being much higher than observed. Specifically, the Belt stars (δ, ϵ, ζ, σ) and λ Ori are displaced by 10 pc from the plane at 450 pc. The exact value chosen for the larger offset only weakly affects the final results; the only requirement is that the offset is significantly larger than 1 pc.
3. Stars not included in Warren & Hesser (1977) or Murdin & Penston (1977) make a negligible contribution to Orion's radiation field. This includes stars down to visual magnitudes of 10–11.

The radiation field caused by Orion's stars at pixel (i, j) is given by

$$U_*(i, j) = \sum_k \frac{L_k}{4\pi[r_k^2(i, j) + d_k^2]} . \tag{6}$$

L_k is the luminosity of star k, $r_k(i, j)$ is the projected distance from star k to pixel (i, j) in the "plane" of the cloud, and d_k is the line-of-sight offset discussed in item 2 above. Figure 17*a* shows the map expressed in units of $L_\odot$ pc^{-2}. A value of 1 $L_\odot$ pc^{-2} means that a sphere with a cross-sectional area of 1 pc^2 receives 1 $L_\odot$ of radiation through 4π steradians.

Another implicit assumption in determining U_* from equation (6) is that there is no extinction between each star k and each pixel (i, j): i.e., $\tau_k(i, j) = 0$. Bally et al. (1991) found it necessary to include extinction effects when estimating the radiation field in their attempts to derive the dust-to-gas ratio. With extinction effects, equation (6) becomes

$$U_*(i, j) = \sum_k \frac{L_k \exp\,[-\tau_k(i, j)]}{4\pi[r_k^2(i, j) + d_k^2]} . \tag{7}$$

Due to a lack of detailed depth perception, there is no unique way to determine $\tau_k(i, j)$. However, we have adopted a treatment such that the resultant U_* map allows a reasonable esimate of the observed $\mathscr{L}$ (12–240 μm) map. The optical depth, $\tau_k(i, j)$, is derived from

$$\tau_k(i, j) = \frac{N_k(i, j)}{1.6 \times 10^{21}\ \text{cm}^{-2}} . \tag{8}$$

$N_k(i, j)$ is the "effective" column density of material between

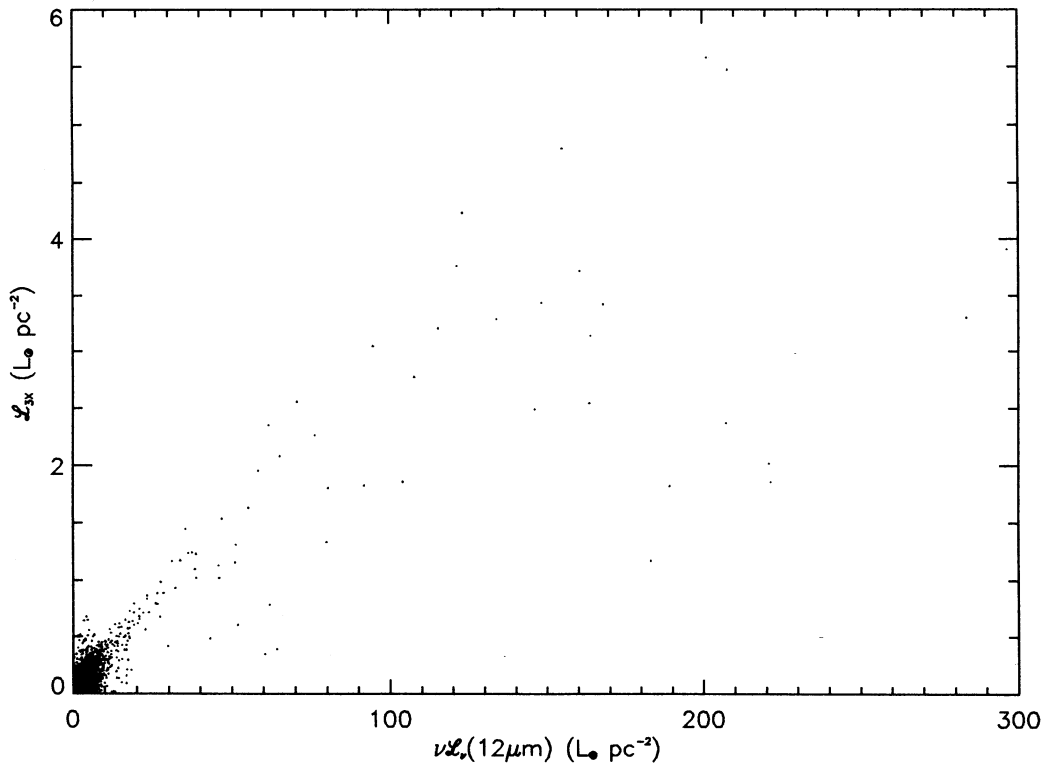

FIG. 16*a*

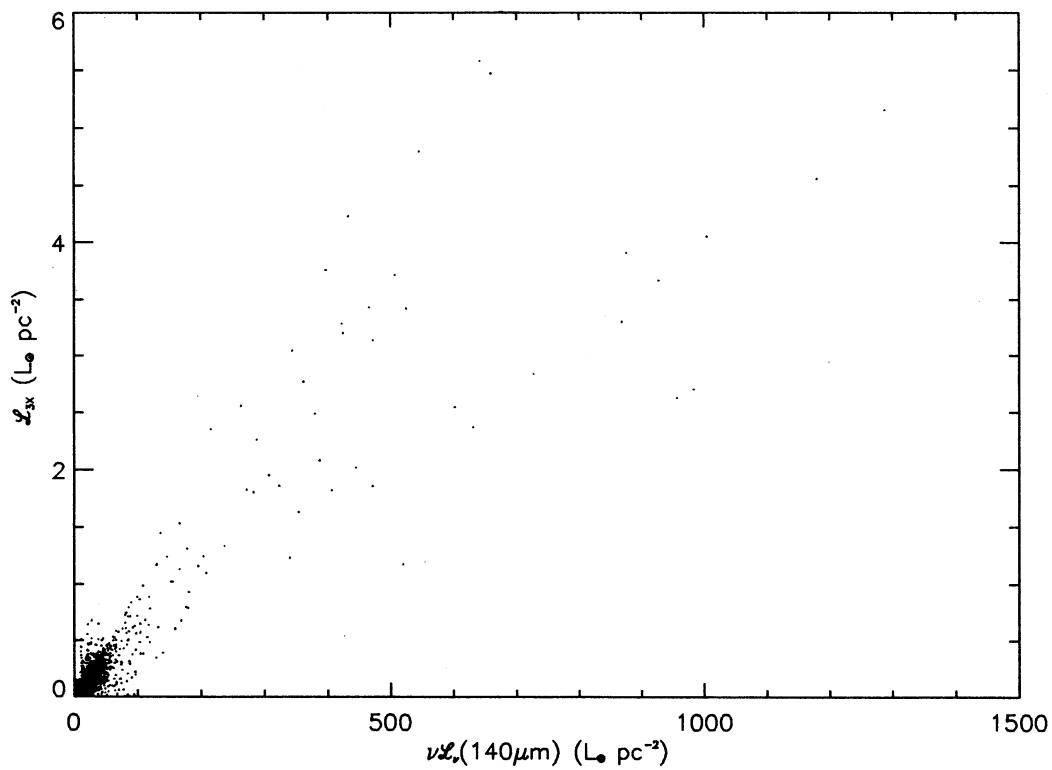

FIG. 16*b*

FIG. 16.—(*a*) The surface luminosity of the 3.5 μm band excess is plotted against $\nu\mathscr{L}_\nu$ at 12 μm for positions within the Orion fields. (*b*) The surface luminosity of the 3.5 μm band excess is plotted against $\nu\mathscr{L}_\nu$ at 140 μm for positions within the Orion fields.

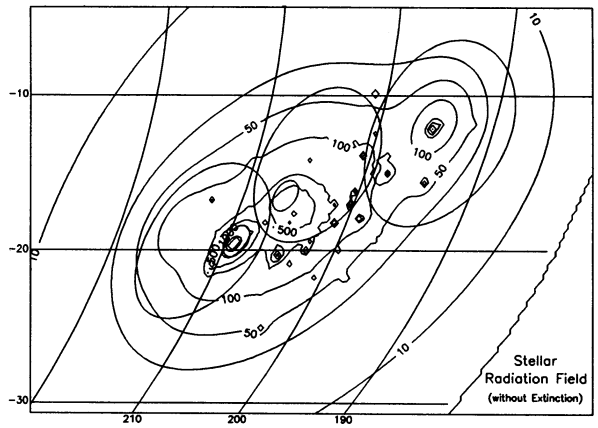

FIG. 17a

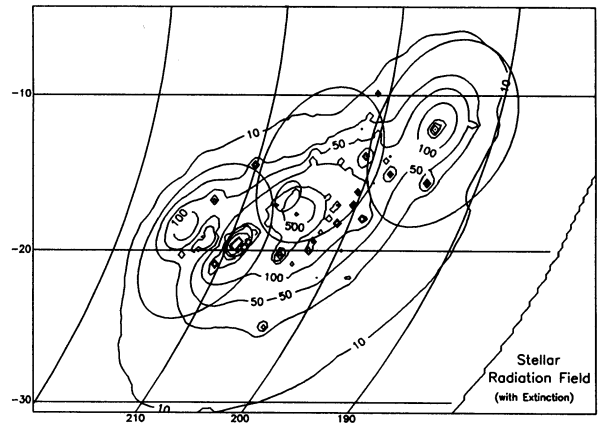

FIG. 17b

FIG. 17.—The inferred spatial distribution of the radiation field caused by the Orion OB1 and λ Ori OB associations is shown. The contour levels are 10, 30, 50, 100, 300, 500, 1000, 3000, and 5000 $L_\odot$ pc^{-2}. (*a*) The effects of extinction are ignored in the determination of the radiation field. (*b*) The effects of extinction are included according to the prescription described in § 4.

pixel (i, j) and star k (across the line of sight in the "plane" of the sky). To estimate $N_k(i, j)$, we must use a reasonable variation of the volume density along the path from star k to pixel (i, j). The volume density variation along a given path is assumed to be identical to that of the observed line-of-sight column density along this path. This treatment is unrealistic because it assumes a constant line-of-sight depth everywhere but is probably more realistic than assuming a constant density everywhere. It follows then that

$$N_k(i, j) = c_v \langle N(\mathrm{H})_{\mathrm{dust}} \rangle r_k(i, j) , \quad (9)$$

where $\langle N(\mathrm{H})_{\mathrm{dust}} \rangle$ is the average of the column densities along the path from star k to pixel (i, j), and c_v is column density to volume density conversion. The $N(\mathrm{H})_{\mathrm{dust}}$ in equation (9) is provided by the column density map (Fig. 8). We created three radiation field maps, each with its own value of c_v: 5×10^{21} cm^{-1}, 5×10^{-20} cm^{-1}, and 5×10^{-19} cm^{-1}.

To choose the correct radiation field map (i.e., choose c_v), we must find which map best reproduces the observed dust luminosity map, $\mathscr{L}_{\mathrm{dust}}$ or $\mathscr{L}$(12–240 μm). Dust luminosity is reemission of the absorbed radiation field. For a blob with effective absorption optical depth, τ, the fraction of incident radiation from all directions that is absorbed is $1 - e^{-\tau}$ (since the transmitted portion is $e^{-\tau}$, by definition of τ). If the blob has column density $N(\mathrm{H})_{\mathrm{dust}}$, then the observed dust surface luminosity is given by

$$\mathscr{L}_{\mathrm{dust}} = (U_* + U_G)\left\{1 - \exp\left[\frac{-N(\mathrm{H})_{\mathrm{dust}}}{1.6 \times 10^{21}\ \mathrm{cm}^{-2}}\, f\right]\right\} , \quad (10)$$

with U_G as the contribution by the GISRF (using $U_G = 50\ L_\odot$ pc^{-2}), and where f is a correction factor that converts the extinction in the V band to an absorption optical depth. The factor f corrects for porosity (i.e., clumping), for the possibility of the effective wavelength of absorption being outside the V band, and for scattering. Notice that when τ (i.e., the argument of the exponential in eq. [10]) is large, the surface brightness is the same as the radiation field. The combination $c_v = 5 \times 10^{-21}$ cm^{-1} and $f = 0.3$ best reproduces the observed dust luminosity. Figure 17*b* shows the radiation field map that includes extinction effects according to the prescription described above.

The best model dust luminosity map and the fractional residuals are shown in Figures 18*a* and 18*b*, respectively. The model $\mathscr{L}_{\mathrm{dust}}$ map (Fig. 18*a*) generally agrees with the observed $\mathscr{L}_{\mathrm{dust}}$ (Fig. 4). However, in the Orion Nebula, NGC 2024, and at the stars κ Ori and λ Ori, the model $\mathscr{L}_{\mathrm{dust}}$ is factors of ~2.8 higher than the observed $\mathscr{L}_{\mathrm{dust}}$, which can be corrected by merely adjusting the offset distances, d_k, by factors ~2–3 for λ Ori, κ Ori, and the stars in the Orion Nebula and NGC 2024. It is possible that, in some cases, these stars are genuinely displaced by a few, to a few tens, of parsecs from the Orion clouds. Nevertheless, the current model dust luminosity map (Fig. 18*a*) and the map of fractional residuals (Fig. 18*b*) suggest that the radiation field map shown in Figure 17*b* is a crude but reasonable representation of the spatial distribution of the radiation fields responsible for heating Orion's dust; for about 70% of the positions within the Orion fields, the model surface luminosities are within 50% of the observed surface luminosities.

The radiation field is compared with the dust temperature in Figure 19. Since we expect $T_{\mathrm{dust}} \propto (U_* + U_G)^{1/(4+\beta)}$, we have plotted arbitrarily scaled curves of $T_{\mathrm{dust}} \propto U_*^{1/6}$ for comparison. We can neglect U_G for $U_* > U_G = 50\ L_\odot$ pc^{-2}, giving T_{dust} to within ~10%. Most of the points demonstrate a rapid rise from $T_d = 15$ K to $T_d \simeq 22$ K for $U_* < 100\ L_\odot$ pc^{-2}; these same positions have low column densities [$N(\mathrm{H})_{\mathrm{dust}} \lesssim 2 \times 10^{21}$ cm^{-2}] and reach high temperatures in weak fields. Figure 19 also demonstrates the association of stars with molecular gas because the positions with high radiation fields ($U_* > 300\ L_\odot$ pc^{-2}) are mostly those dominant in molecular gas.

In § 3.3, we found temperature dependence for the apparent dust-to-gas mass ratio $N(\mathrm{H})_{\mathrm{dust}}/N(\mathrm{H\ I} + 2\mathrm{H}_2)$. A similar dependence should exist between $N(\mathrm{H})_{\mathrm{dust}}/N(\mathrm{H\ I} + 2\mathrm{H}_2)$ and the radiation field. The radiation field is compared with the normalized dust-to-gas ratio, $N(\mathrm{H})_{\mathrm{dust}}/N(\mathrm{H\ I} + 2\mathrm{H}_2)$, in Figures 20*a* and 20*b*. In the map of Figure 20*a*, the thick contour encloses the region where the radiation field due to the OB associations dominates over the GISRF. Positions with $N(\mathrm{H})_{\mathrm{dust}}/N(\mathrm{H\ I} + 2\mathrm{H}_2) < 1$ occur largely inside this contour; indeed, the $N(\mathrm{H})_{\mathrm{dust}}/N(\mathrm{H\ I} + 2\mathrm{H}_2) = 1$ boundary seems to follow the $U_* = U_G = 50\ L_\odot$ pc^{-2} contour (except in the λ Ori field, where background subtraction is a problem). The plot of

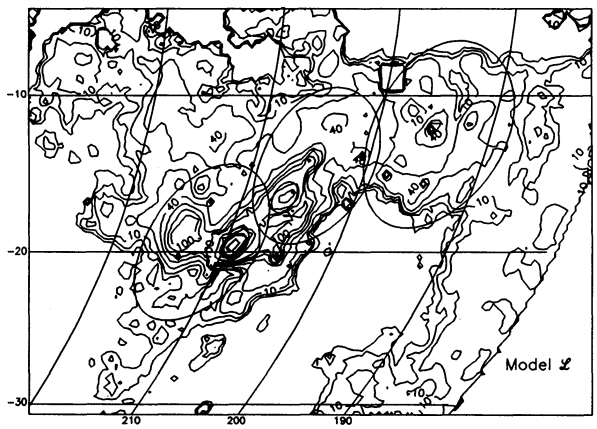

FIG. 18*a*

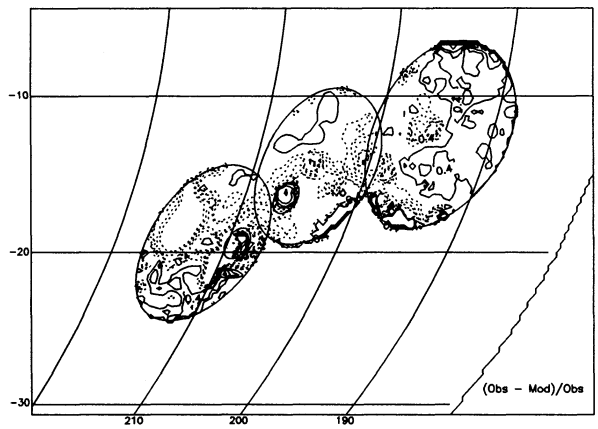

FIG. 18*b*

FIG. 18.—(*a*) The map of the dust luminosity modeled from the radiation field map and the column density map is shown. Contour levels are the same as in Fig. 8. See § 4.1 for details. (The α Ori data have been excised from the map.) (*b*) The map of fractional residuals is shown. The fractional residuals represent the (observed − model)/observed. The levels of the dashed contours are −1, −0.8, −0.6, −0.4, and −0.2, and the levels of the solid contours are +0.2, +0.4, +0.6, +0.8, and +1.0. See § 4.1 for details.

$N(\mathrm{H})_{\mathrm{dust}}/N(\mathrm{H\ I} + 2\mathrm{H}_2)$ versus U_* is given in Figure 20*b*. This plot is similar to that of $N(\mathrm{H})_{\mathrm{dust}}/N(\mathrm{H\ I} + 2\mathrm{H}_2)$ versus T_d (Fig. 14) and may have a similar explanation: the positions of stronger radiation field have a greater temperature variation along the line of sight, leading to a systematic underestimate of dust-derived column densities using the single-temperature assumption.

4.2. *Proportion of Dust Luminosity from GISRF-heated dust*

The dust luminosity is attributable to dust heated by both the GISRF and by the Orion stars. In this section, we estimate what fraction of the dust luminosity is caused by each.

From modeling the dust luminosity map, we know that the absorption optical depth is approximated by $N(\mathrm{H})_{\mathrm{dust}}\,f/$

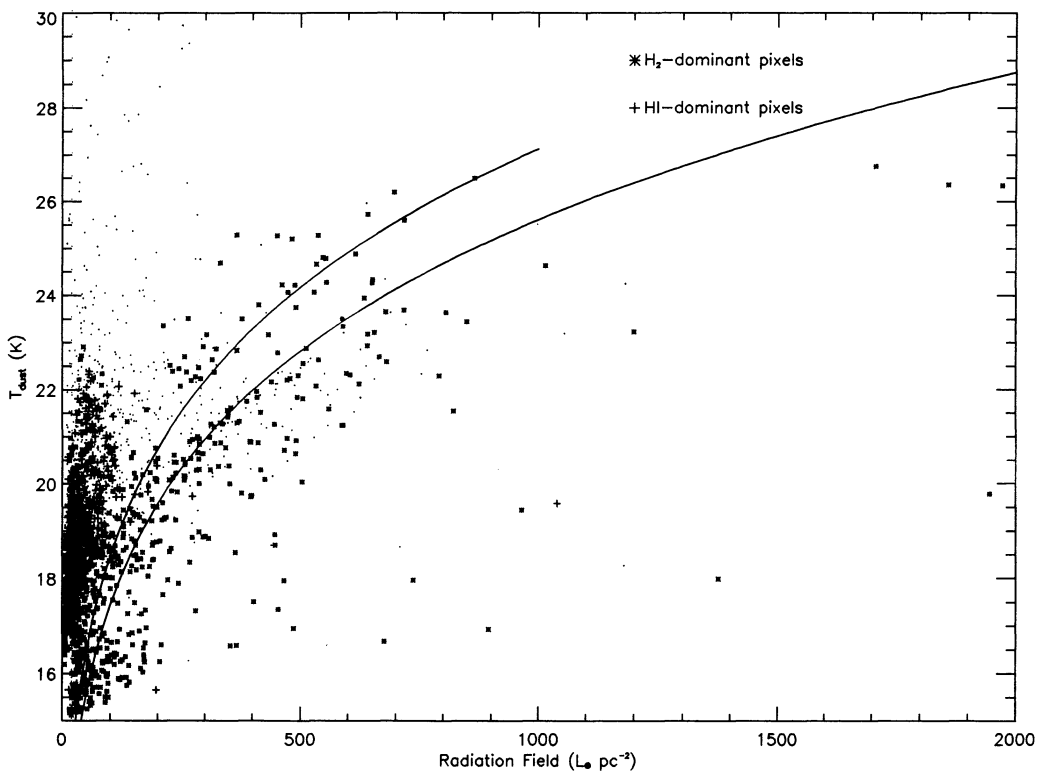

FIG. 19.—The 140/240 μm color temperature, T_{dust}, is plotted as a function of the Orion stellar radiation field strength, U_*, for positions within the Orion fields. Data points representing molecular (or atomic) gas dominant positions are marked with asterisks (plus signs). A given pixel is considered to be dominant in molecular (or atomic) gas if the mass of molecular (or atomic) gas within the pixel is more than double that of the atomic (or molecular) gas. Arbitrarily scaled solid curves depicting $T_{\mathrm{dust}} \propto U_*^{1/6}$ are plotted for comparison.

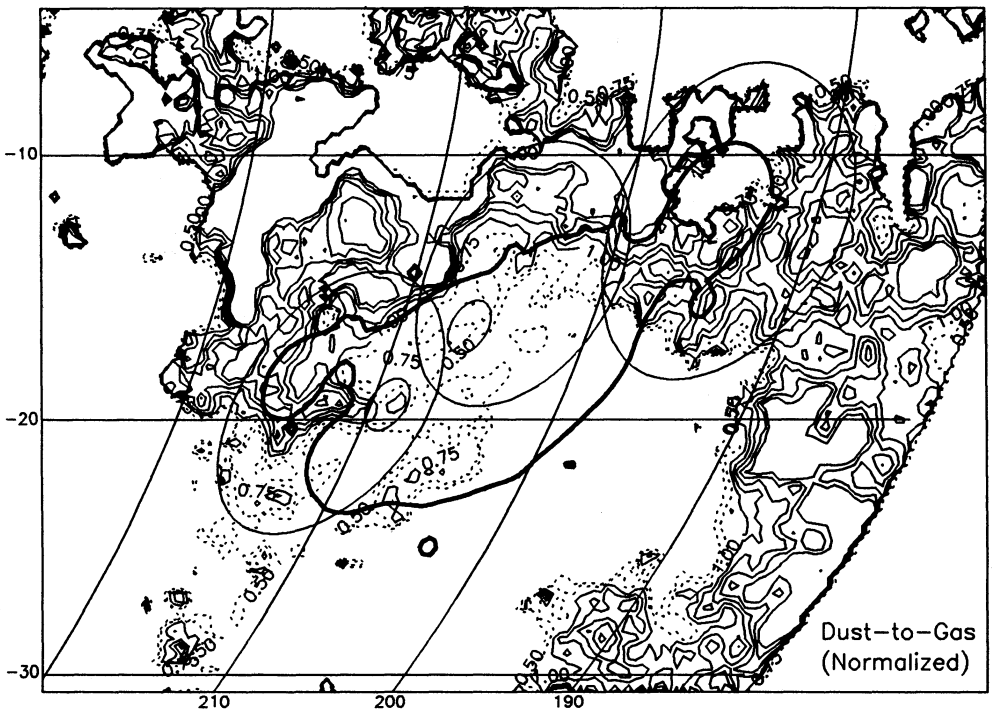

FIG. 20*a*

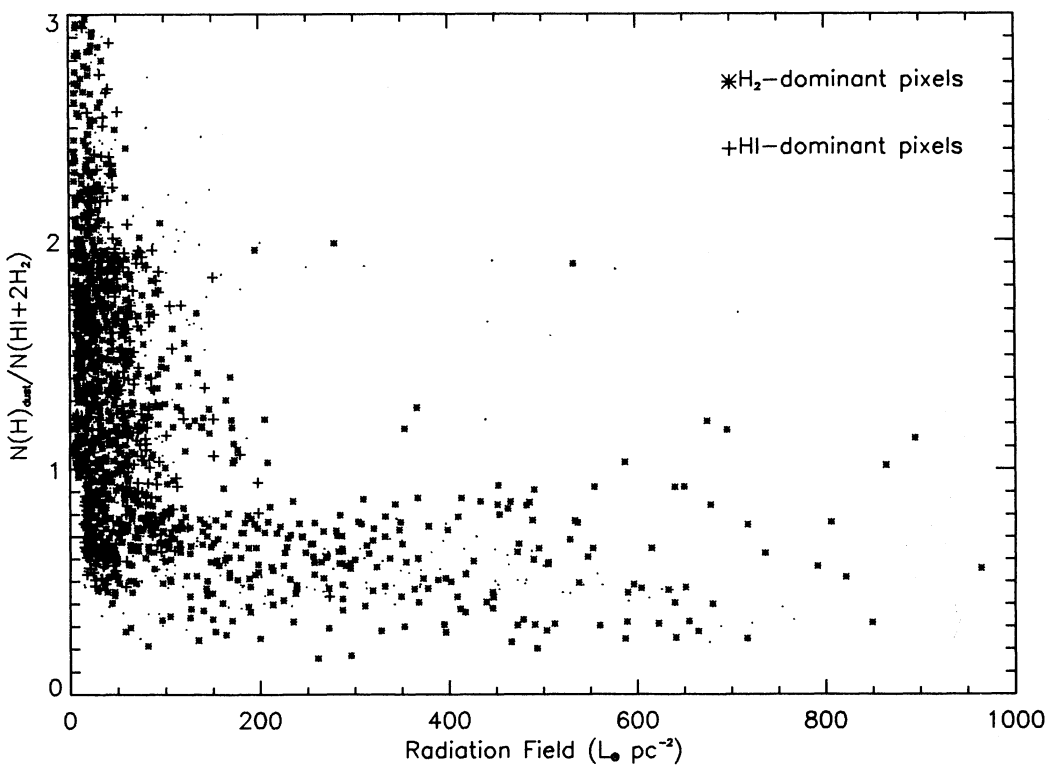

FIG. 20*b*

FIG. 20.—(*a*) The spatial distribution of the normalized dust-to-gas ratio, $N(\mathrm{H})_{\mathrm{dust}}/N(\mathrm{H\ I} + 2\mathrm{H}_2)$, is illustrated. The thick contour represents the radiation field due to Orion stars at a level of 50 $L_{\odot}$ pc^{-2}. The dashed contours represent positions where $N(\mathrm{H})_{\mathrm{dust}}/N(\mathrm{H\ I} + 2\mathrm{H}_2) < 1$. The $N(\mathrm{H})_{\mathrm{dust}}/N(\mathrm{H\ I} + 2\mathrm{H}_2)$ contour levels are 0.50, 0.75, 1.00, ... , 2.00. (*b*) $N(\mathrm{H})_{\mathrm{dust}}/N(\mathrm{H\ I} + 2\mathrm{H}_2)$ is plotted against the radiation field due to the Orion stars for positions within the Orion fields. Data points representing molecular gas (or atomic gas) dominant positions are marked with asterisks (or plus signs).

TABLE 5

PROPORTION OF DUST LUMINOSITY CAUSED BY GISRF-HEATED DUST

	L_{GISRF}/L_{dust}					
METHOD	Orion Nebula	Orion A	NGC 2024	Orion B	λ Ori	Combined[a]
1[b]	0.02	0.17	0.05	0.27	0.45	0.24
2[c]	0.15	0.40	0.23	0.46	0.95	0.36

[a] Combined Orion A + Orion B + λ Ori field.
[b] Using absorption depth estimated from modeling the dust luminosity and assumed GISRF; see § 4.2.
[c] From modeling the spectral energy distribution; see § 4.2.

1.6×10^{21} cm^{-2}, with $f = 0.3$. The surface luminosity of dust heated by the GISRF is then given by (see eq. [10])

$$\mathscr{L}_{GISRF} = U_G \left\{ 1 - \exp\left[\frac{-N(\mathrm{H})_{dust}}{1.6 \times 10^{21}\ \mathrm{cm}^{-2}} f \right] \right\} . \quad (11)$$

Equation (11) and the observed dust luminosity gives us the fraction due to GISRF-heated dust (see method 1 in Table 5): 24% for the combined Orion A + Orion B + λ Ori field. If we assumed $f = 1$, we would obtain L_{GISRF}/L_{dust} of 50% for the combined Orion A + Orion B + λ Ori field. If we assumed $f = 0.1$, using the U_* map that neglects extinction (Fig. 17*a*) L_{GISRF}/L_{dust} would be 10%.

The shapes of spectral distributions themselves can provide estimates of the fraction of dust luminosity caused by dust heated mainly by the GISRF. The spectral distribution of the λ Ori field (Fig. 5) resembles much more closely that of the Galactic plane than do the spectral distributions of the Orion A or Orion B fields. One might then expect a larger percentage of the dust luminosity from GISRF-heated dust in the λ Ori fields than in the Orion A or Orion B fields, which is consistent with the results in Table 5 (method 2). We used the models of Désert et al. (1990) to investigate this in more detail, combining their dark cloud models (GISRF with extinction) and their O5 star dust-heated models so as to match the observed spectral distributions. The Désert et al. model intensities are listed for a few wavelengths from 2.2 μm to 800 μm in a number of different cases. Their dark cloud models give the expected spectral distributions for dust heated by the GISRF and shielded by varying levels of extinction, from $A_v = 0.0$ to $A_v = 5.0$. Their O5 star–heated models give the expected spectral distributions for dust heated by an O5 star at varying distances from the dust. For the observed spectral distribution of each Orion field, we combined one dark cloud model spectral distribution with one O5 star–heated model and varied the column densities of the two model distributions until their sum approximated the observed distribution. Then a new dark cloud model and a new O5 star–heated model combination is fitted to the data. (We fitted the Désert et al. models only to the 25–240 μm data because these models would not simultaneously fit near-IR and mid-IR to far-IR intensities.) The model pair that best fits the observed spectral distribution of the field is shown in Figure 21 for each field. The best fit is used to determine the fraction of dust luminosity caused by GISRF-heated dust (see Table 6). As listed in Table 5, the GISRF-heated dust accounts for ~40% of the dust luminosity from Orion. This 40% is the result from the best-fitting model pair, but all model pairs give $L_{GISRF}/L_{dust} > 16\%$ for Orion (i.e., Orion A + Orion B + λ Ori fields). Applying the same modeling technique to the Galactic plane, for latitudes within 15° of the plane, yields ~80% as the fraction of the Galaxy's dust luminosity resulting from GISRF-heated dust.

Both methods for determining the proportion of dust thermal luminosity attributable to dust heating mainly by the GISRF have their shortcomings. The method that uses the dust thermal absorption optical depth, determined from the radiation field and modeling the $\mathscr{L}_{dust}$ map, uses a global correction factor, f, and by necessity, ignores the three-dimensional dust distribution. (Indeed, Brown et al. 1994 estimate the near side of the Orion clouds to be 320 pc distant, and the far side to be 500 pc.) Applying physical models to the spectral distribution must account for the nonuniqueness of the fit, in that different model pairs (i.e., one GISRF model and one O5 star–heated model) with different resultant L_{GISRF}/L_{dust}

TABLE 6

SPECTRAL ENERGY DISTRIBUTION MODEL RESULTS

	FIELDS					
PARAMETER	Orion Nebula	Orion A	NGC 2024	Orion B	λ Ori	Combined[b]
χ^2_ν	0.06	0.14	0.20	1.3	0.21	0.15
Dark Cloud Parameters						
A_v	0	0	0	1	0	1
Mass ($M_\odot$)	3.3×10^4	1.3×10^5	2.1×10^4	1.8×10^5	8.1×10^4	5.0×10^5
O5-Heated Model Parameters						
Distance[c] (pc)	0.3	0.3	0.17	0.1	0.17	0.17
Mass ($M_\odot$)	7.9×10^2	8.1×10^2	9.2×10^2	3.5×10^2	5.6×10^1	5.0×10^3

[a] See the dark cloud models and O5 star–heated models of Désert et al. (1990).
[b] Combined Orion A + Orion B + λ Ori field.
[c] Related to the Désert et al. dilution factor, such that distance (pc) = (dilution)$^{-0.5}$.

1996ApJ...456..566W

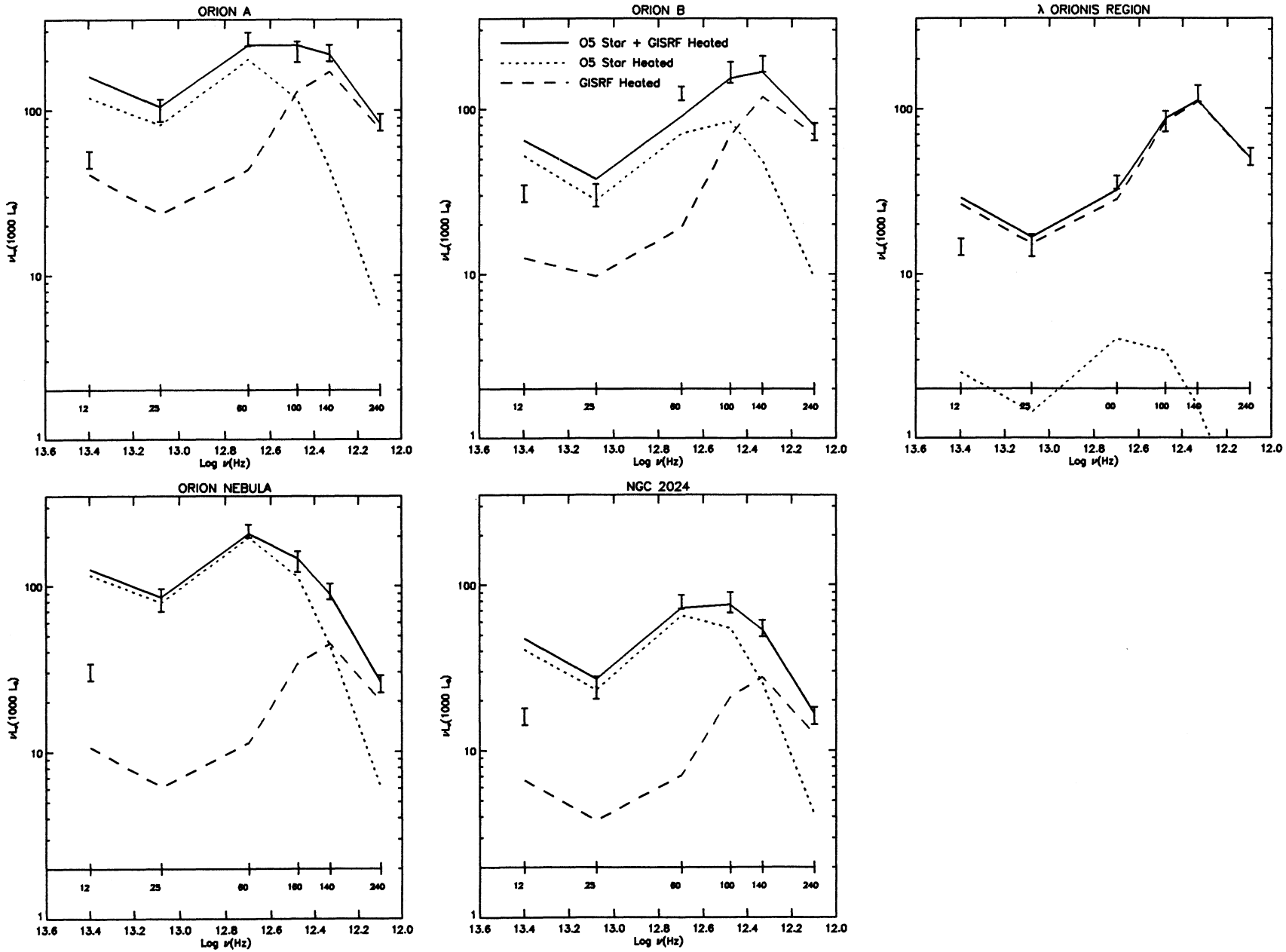

FIG. 21.—The model and observed spectral energy distributions are shown for the five Orion fields. Error bars on the data points represent the absolute calibration uncertainties. Solid, dotted, and dashed curves represent the model spectral energy distributions using the models of Désert et al. (1990). The solid curve gives the best fit to the data points using a combination of model dust heated by an O5 star (*dotted curve*) and model dust heated by the general interstellar radiation field (*dashed curve*); see § 4.2 for details. The models were fitted only to the 25–240 μm data. Notice how the models overestimate the 12 μm luminosity.

can still fit the same data reasonably well. Therefore, disagreement between the two methods is not surprising. The best estimate of the proportion of dust thermal luminosity caused by GISRF-heated dust lies in the range 24%–36%. This is the first global estimate of $L_{\rm GISRF}/L_{\rm dust}$ for the Orion region with such a comprehensive data set.

5. IMPLICATIONS FOR EXTERNAL GALAXY OBSERVATIONS

Even though the clouds of Orion are very small on galactic scales, their proximity to the Earth has allowed them to be modeled in great detail, thereby allowing a rough extrapolation to galactic scales. Gifen that the region studied in this paper is more than 200 pc in size, applying the results of this paper to infrared studies of external galaxies may not be unreasonable. The three large fields (Orion A + Orion B + λ Ori) fit collectively inside a 1′ beam if placed at a distance of 1 Mpc. This naturally raises the question of what we would infer for this region if the Orion dust, gas, and stars were plucked out of our Galaxy, placed in another galaxy 1 Mpc away, and observed with a 1′ beam. If our new spatial resolution allows us to barely resolve this extragalactic Orion, but we have good signal-to-noise ratios in all bands and we retain knowledge of the OB associations, it turns out that most of our results are little affected. This was tested by using only the intensities averaged over all three large fields. The derived dust thermal luminosity, L(12–240 μm), is identical to that derived from the full-resolution maps (since this derivation is linear). The mass determined from the averaged I_ν(140 μm) and I_ν(240 μm) intensities underestimates that determined from the column density map by only 15%. A global average underestimates the mass because the positions with warm dust are averaged with positions of cold dust, overestimating the effective temperature and, hence, underestimating the column density (see § 3.3.2). The two methods used to estimate the fraction of dust luminosity caused by GISRF-heated dust (see § 4.2) can be carried out pixel by pixel in the full-resolution maps or on the globally averaged intensities, and results are largely unchanged (i.e., $L_{\rm GISRF}/L_{\rm dust}$ is in the range of 24%–45%).

Dust-to-gas mass ratios estimated from 60 and 100 μm *IRAS* data in external galaxies are lower by an order of magnitude from the typical Galactic ratio (e.g., see Devereux & Young 1990). This has prompted the suggestion of a cold, ~15–20 K, dust component supposedly not sampled by the *IRAS* observations, but observable at longer wavelengths (e.g., Sievers et al. 1994; Guélin et al. 1993; Devereux & Young 1990). However, with the benefit of the longer wavelength observations, we find that a ratio of *any* pair of the 100, 140, and 240 μm intensities gives the *same* temperature to within ~2 K, and that temperature is usually 18 K. In other words, the 100 μm observations *already* sample a cool (~18 K) component. The 60 and 100 μm mass estimates, which assume thermal equilibrium, are too low because the 60 μm emission has a strong contribution from stochastically heated grains (see Désert et al. 1990, and references therein; Sodroski et al. 1994; § 3.3). Of course, observations at 100 μm do not rule out the much colder dust, ~5 K, inferred from the *COBE*/FIRAS observations in our Galaxy (Reach et al. 1995; Wright et al. 1991).

An important question often addressed by infrared studies of external galaxies is the fraction of the dust heating caused by ultraviolet (UV) radiation, which is roughly equivalent to the fraction of dust heating caused by early-type stars. Estimates of this fraction fall in the neighborhood of 40%–80% (e.g., see Lisenfield & Völk 1993; Madden et al. 1993; Rice et al. 1990; Xu 1990). Results of the previous section provide estimates of the UV fraction for Orion's dust heating that lie in the upper end of this range. The stars dominating the energetics of Orion (δ, θ^1, ι, ϵ, σ, ζ, λ, and κ) all have spectral types very near O9, implying effective temperatures near 3×10^4 K, in turn implying that 90% of their luminosity is at UV wavelengths. The fraction of the interstellar radiation field at UV wavelengths is about 20% (see Table A3 of Mathis et al. 1983). Given that 64%–76% of the dust luminosity in Orion is caused by Orion's stars, with the rest caused by a general interstellar radiation field, 65%–73% of the dust luminosity in Orion is attributable to dust heated by UV photons. For this derivation, we have assumed that UV wavelengths are no longer than 400 nm. If we instead adopt 200 nm as the long-wavelength limit, then the fraction of Orion's dust luminosity caused by UV-heated dust is 48%–55%, which is closer to the lower end of the range of estimates for external galaxies. Note that the percentages given above neglect the greater dust heating per photon energy that occurs for UV photons than for visible light photons. For regions that are optically thick both in the UV and in the V band, no correction is necessary. In the Orion fields, more than 70% of the dust luminosity originates from regions with $A_v \geq 1$. Because the dust luminosity comes primarily from optically thick regions, we estimate that the stated percentage of dust luminosity in Orion attributable to dust heated by UV photons must be corrected upward by only a few (i.e., $\lesssim 5$) percentage points.

The fraction of the total stellar luminosity that appears at infrared wavelengths in Orion is comparable to that of the nearby spiral galaxy M33. *IRAS* observations of M33 imply that its total dust luminosity (integrated infrared luminosity) is ~20% of the total stellar luminosity (Rice et al. 1990). This compares to the 25%–30% estimated for Orion, obtained from the ratio of the dust luminosity of local stars, 0.64–0.76 of the total dust luminosity or $6–8 \times 10^5\ L_\odot$, to the total stellar luminosity of $2.5 \times 10^6\ L_\odot$. However, it should be remembered that M33 has a very low infrared activity compared with other *IRAS* galaxies (see de Jong et al. 1984; Soifer et al. 1984). It is interesting to note that the Leisawitz & Hauser (1988) observations of molecular clouds surrounding OB associations may account for the relative dust luminosity to stellar luminosity ratios: the proportion of O stars embedded in their parental clouds may be the same in M33 as in Orion but less than those in other, more infrared-active galaxies.

It is also possible to use the Orion data to estimate the ratio of dust thermal luminosity in a spiral arm to that in the interarm region for a spiral galaxy. This arm-to-interarm ratio can, for example, constrain estimates of the effects of the spiral density wave on star formation (e.g., Roberts & Stewart 1987). The OB stars in the spiral arms enhance the radiation field beyond what it would have been in the absence of the OB stars. In Orion, we found this enhancement to be ~2–4 (i.e., $L_{\rm dust}/L_{\rm GISRF} \simeq 2$–4). Therefore, averaged over 100 pc scales, the ratio of arm-to-interarm *surface* luminosities, $\mathscr{L}$(12–240 μm), is expected to be 2–4. For comparison, the arm-interarm contrast in the CO $J = 1 \rightarrow 0$ line for the spiral galaxy M51 is ~2–5 (Adler et al. 1992; Vogel, Kulkarni, & Scoville 1988).

6. CONCLUSIONS

We have presented data covering much of the Orion constellation in 10 wavelength bands spanning the wavelengths from 1.25 to 240 μm, along with a simple analysis of those data. The

near-IR (1.25, 2.2, 3.30, and 4.9 μm) spectral distributions of the Orion Nebula and NGC 2024 indicate the presence of hot ($T \sim$ few $\times 10^2$ K) dust emission in the near-IR bands, both because of large $I_\nu(4.9\ \mu m)/I_\nu(1.25\ \mu m)$ ratios and because of a substantial excess in the 3.5 μm band. For the Orion Nebula, at least $\sim 30\%$ of this excess is caused by the 3.3 μm line of the PAH molecule. The total luminosity from dust (from 12 to 240 μm) throughout the Orion A, Orion B, and λ Ori fields, covering 16,900 pc^2, is $\sim 10^6\ L_\odot$. This dust luminosity is 40% of the luminosity of the Ori OB1 and λ Ori OB associations. The luminosity in the 12–100 μm range covered by *IRAS* is 60% of the total 12–240 μm dust luminosity, which is consistent with the prediction of Boulanger & Pérault (1988). We estimate that 24%–36% of the dust luminosity is attributable dust heated mainly by the general interstellar radiation field (GISRF), with the rest coming from dust heated by the Orion OB1 and Y Ori OB associations.

The masses for the Orion A, Orion B, and λ Ori fields estimated from the 140 and 240 μm intensities and an assumed opacity–to–column density ratio $[\tau(100\ \mu m)/N(\mathrm{H\ I} + 2\mathrm{H}_2) = 7 \times 10^{-25}\ \mathrm{cm}^2]$, total $3 \times 10^5\ M_\odot$. The masses for the individual fields are reasonably consistent with those determined from CO $J = 1 \rightarrow 0$ and H I 21 cm observations, suggesting a roughly constant $\tau(100\ \mu m)/N(\mathrm{H\ I} + 2\mathrm{H}_2)$ across the Orion region. However, the apparent dust-to-gas ratio, derived from an assumed single-temperature dust model, shows a variation with 140/240 μm color temperature that is explained, in part, by a temperature-dependent systematic error in the dust column density derivation. Nevertheless, to within a factor of 2, the dust-to-gas ratio is constant from position to position. We also confirm the results of Bally et al. (1991), who found that the 60 and 100 μm intensities include a substantial contribution from small stochastically heated grains. Thus, the $I_\nu(60\ \mu m)/I_\nu(100\ \mu m)$ ratio overestimates the temperature of the large ($\gtrsim 0.01$ μm) dust grains that dominate the mass. In contrast, any pair of the 100 μm, 140 μm, or 240 μm intensities gives reasonable dust-to-gas ratios and a consistent temperature, usually 18–20 K, when using an emissivity index of $\beta = 2.0$. This suggests that the 100, 140, and 240 μm emission largely arises in a single-temperature component. Even if β is assumed to be different from 2.0, but is a value that is consistent with the FIRAS data, the 140 and 240 μm color temperature is still lower than that for 60 and 100 μm.

All the above conclusions would have been obtained if the stars and clouds of Orion were placed at the distance of a nearby galaxy (~ 1 Mpc) and observed in the DIRBE wavelength bands in an $\sim 1'$ beam with the same signal-to-noise ratio. Further, it is not too unreasonable to suppose that the stars and clouds in a spiral galaxy's arms could be represented by a series of Orion star and cloud complexes. Since the Orion stars enhance the dust luminosity by factors of 2–4 over that expected from the GISRF alone, one would expect the surface luminosity (in $L_\odot$ pc^2) in the arms (for λ = 12–240 μm) to be 2–4 times that in the interarm regions, averaged over 100 pc scales.

Future research, with the aid of models that can reproduce near-IR, mid-IR and far-IR intensities *simultaneously*, should be capable of constraining details of the radiation field and/or the three-dimensional structure of the dust and gas.

The authors gratefully acknowledge the efforts of the DIRBE data processing and validation teams in producing the high-quality data sets used in this investigation. We also thank the *COBE* Science Working Group for helpful comments on the manuscript. We are grateful to J. L. Jonas for allowing us to use data from the Rhodes/HartRAO Survey prior to publication. This work was largely carried out while W. F. W. held a National Research Council-NASA/GSFC Research Associateship and then held a position as a Visiting Scientist with the Universities Space Research Association. The work was completed while W. F. W. was a Title A Researcher at the Instituto Nacional de Astrofisica, Optica y Electronia.

REFERENCES

Adler, D. S., Lo, K. Y., Wright, M. C. H., Rydbeck, G., Plante, R. L., & Allen, R. J. 1992, ApJ, 392, 497
Andriesse, C. D. 1974, A&A, 37, 257
Arendt, R., et al. 1994, ApJ, 425, L25
Balick, B. 1974, PASP, 86, 616
Bally, J., Langer, W. D., & Liu, W. 1991, ApJ, 383, 645
Berkhuijsen, E. M. 1972, A&AS, 5, 263
Blaauw, A. 1964, ARA&A, 2, 213
Bloemen, H., et al. 1984, A&A, 139, 37
———. 1994, A&A, 281, L5
Boggess, N., et al. 1992, ApJ, 397, 420
Boulanger, F., Beichman, C., Désert, F.-X., Helou, G., Pérault, M., & Ryter, C. 1988, ApJ, 332, 328
Boulanger, F., & Pérault, M. 1988, ApJ, 330, 964
Brown, A. G. A., de Geus, E. J., & de Zeeuw, P. T. 1994, A&A, 289, 101
Chin, G. 1978, Ph.D. thesis, Columbia University
Chen, H., & Tokunaga, A. T. 1994, ApJS, 90, 149
Chromey, F. R., Elmegreen, B. G., & Elmegreen, D. M. 1989, AJ, 98, 2203
COBE DIRBE Explanatory Supplement 1995, ed. M. G. Hauser, T. Kelsall, D. Leisawitz, & J. Weiland, in preparation
Dame, T. M. 1993, in AIP Conf. Proc. 278, Back to the Galaxy, ed. Stephen S. Holt & Frances Verter (New York: AIP), 267
Dame, T. M., et al. 1987, ApJ, 322, 706
de Jong, T., Clegg, P. E., Soifer, B. T., Rowan-Robinson, M., Habing, H. J., Houck, J. R., Aumann, H. H., & Raimond, E. 1984, ApJ, 278, L67
Désert, F.-X., Boulanger, F., & Puget, J. L. 1990, A&A, 237, 215
Devereux, N. A., & Young, J. S. 1990, ApJ, 359, 42
Draine, B. T., & Lee, H. M. 1984, ApJ, 285, 89
Geballe, T. R., Lacy, J. H., Persson, S. E., McGregor, P. J., & Soifer, B. T. 1985, ApJ, 292, 500
Geballe, T. R., Tielens, A. G. G. M., Allamandola, L. J., Moorhouse, A., & Brand, P. W. J. L. 1989, ApJ, 341, 278
Genzel, R., & Stutzki, J. 1989, ARA&A, 27, 41
Giard, M., Lamarre, J. M., Pajot, F., & Serra, G. 1994, A&A, 286, 203
Giard, M., Pajot, F., Lamarre, J. M., Serra, G., & Caux, E. 1989, A&A, 215, 92
Goudis, C. 1982, The Orion Complex: A Case Study of Interstellar Matter (Boston: Reidel)
Green, D. A. 1991, MNRAS, 253, 350
Guélin, M., Zylka, R., Mezger, P. G., Haslam, C. G. T., Kreysa, E., Lemke, R., & Sievers, A. W. 1993, A&A, 279, L37
Haslam, C. G. T., Quigley, M. J. S., & Salter, C. J. 1970, MNRAS, 147, 405
Hauser, M. G. 1993, in AIP Conf. Proc. 278, Back to the Galaxy, ed. S. S. Holt & F. Verter (New York: AIP), 201
Hauser, M. G., et al. 1991, in AIP Conf. Proc. 222, After the First Three Minutes, ed. S. Holt, C. Bennett, & V. Trimble (New York: AIP), 161
Heiles, C., & Habing, H. J. 1974, A&AS, 14, 1
IRAS Catalogs and Atlases: Explanatory Supplement. 1988, ed. C. A. Beichman, G. Neugebauer, H. J. Habing, P. E. Clegg, & T. J. Chester (Washington, DC: GPO)
Jonas, J. L., Baart, E. E., & Nicolson, G. D. 1995, in preparation
Jonas, J. L., de Jager, G., & Baart, E. E. 1985, A&AS, 62, 105
Kessler, M. F. 1992, in Infrared Astronomy with ISO, ed. Th. Encrenaz & M. F. Kessler (Commack: Nova), 3
Kutner, M. L., Tucker, K. D., Chin, G., & Thaddeus, P. 1977, ApJ, 215, 521
Léger, A., & Puget, J. L. 1984, A&A, 137, L5
Leisawitz, D., & Hauser, M. G. 1988, ApJ, 332, 954
Lisenfeld, U., & Völk, H. J. 1993, in Star Formation, Galaxies, and the Interstellar Medium, ed. J. Franco, F. Ferrini, & G. Tenorio-Tagle (Cambridge: Cambridge Univ. Press), 75
Lynds, B. T. 1962, ApJS, 7, 1
Maddalena, R. J., Morris, M., Moscowitz, J., & Thaddeus, P. 1986, ApJ, 303, 375
Madden, S. C., Geis, N., Genzel, R., Herriman, F., Jackson, J., Poglitsch, A., Stacey, G. J., & Townes, C. H. 1993, ApJ, 407, 579
Maloney, P. R., & Black, J. H. 1988, ApJ, 325, 389
Mathis, J. S., Mezger, P. G., & Panagia, N. 1983, A&A, 128, 212

Mathis, J. S., Rumpl, W., & Nordsieck, K. H. 1977, ApJ, 217, 425
Matsumoto, T. 1993, in Adv. Space. Res. 13, ed. J. Trümper, C. Cesarsky, G. G. C. Palumbo, & G. F. Bignami (Oxford: Pergamon), (12) 495
Mazzarella, J. M., Voit, G. M., Soifer, B. T., Matthews, K., Graham, J. R., Armus, L., & Shupe, D. 1994, AJ, 107, 1274
Mead, K. N., & Kutner, M. L. 1988, ApJ, 330, 399
Mizutani, K., Suto, H., & Maihara, T. 1994, ApJ, 421, 475
Mouri, H., Kawara, K., Taniguchi, Y., & Nishida, M. 1990, ApJ, 356, L39
Murdin, P., & Penston, M. V. 1977, MNRAS, 181, 657
Pearson, F. 1990, Map Projections: Theory and Applications (Boca Raton: CRC Press Inc.)
Reach, W. T., et al. 1995, ApJ, 451, 188
Reich, W. 1978, A&A, 64, 407
Rice, W., Boulanger, F., Viallefond, F., Soifer, B. T., & Freedman, W. L. 1990, ApJ, 358, 418
Rieke, G. H., & Lebofsky, M. J. 1985, ApJ, 288, 618
Roberts, W. W., & Stewart, G. R. 1987, ApJ, 314, 10
Sakamoto, S., Hayashi, M., Hasegawa, T., Handa, T., & Oka, T. 1994, ApJ, 425, 641
Scoville, N. Z., Kleinman, S. G., Hall, D. N. B., & Ridgway, S. T. 1983, ApJ, 275, 201
Seki, J., & Yamamoto, T. 1980, Ap&SS, 72, 79
Sellgren, K. 1981, ApJ, 245, 138
Sellgren, K., Tokunaga, A. T., & Nakada, Y. 1990, ApJ, 349, 120
Sievers, A. W., Reuter, H.-P., Haslam, C. G. T., Kreysa, E., & Lemke, R. 1994, A&A, 281, 681
Silverberg, R. F., et al. 1993, in Proc. SPIE Conf. 2019, Infrared Spaceborne Remote Sensing, ed. M. S. Scholl (Bellingham: SPIE), 180
Snow, T. P., & Morton, D. C. 1976, ApJS, 32, 429
Sodroski, T. J., et al. 1994, ApJ, 428, 638
Soifer, B. T., et al. 1984, ApJ, 278, L71
Spitzer, L. 1978, Physical Processes in the Interstellar Medium (New York: Wiley)
Tenorio-Tagle, G. 1979, A&A, 71, 59
Tucker, K. D., Kutner, M. L., & Thaddeus, P. 1973, ApJ, 186, L13
van den Bergh, S. 1966, AJ, 71, 990
Vogel, S. N., Kulkarni, S. R., & Scoville, N. Z. 1988, Nature, 334, 402
Warren, W. H., & Hesser, J. E. 1977, ApJS, 34, 115
———. 1978, ApJS, 36, 497
Wright, E. L., et al. 1991, ApJ, 381, 200
Xu, C. 1990, ApJ, 365, L47
Zhang, C. Y., & Green, D. A. 1991, AJ, 101, 1006
Zhang, C. Y., Laureijs, R. J., Chlewicki, G., Clark, F. O., & Wesselius, P. R. 1989, A&A, 218, 231
Zuckerman, B. 1973, ApJ, 183, 863